

Comparing results from a physical model with satellite and in situ observations to determine whether biomass burning aerosols over the Amazon brighten or burn off clouds

John E. Ten Hoeve,¹ Mark Z. Jacobson,¹ and Lorraine A. Remer²

Received 16 September 2011; revised 14 March 2012; accepted 15 March 2012; published 26 April 2012.

[1] Biomass burning (BB) aerosol particles affect clouds through competing microphysical and radiative (semi-direct and cloud absorption) effects, each of which dominates at different degrees of aerosol loading. Here, we analyze the influence of competing aerosol effects on mixed-phase clouds, precipitation, and radiative fields over the Amazon with a climate-air pollution-weather forecast model that treats aerosol-cloud-radiative interactions physically. Extensive comparisons with remotely sensed observations and in situ measurements are performed. Both observations and model results suggest an increase in cloud optical depth (COD) with increasing aerosol optical depth (AOD) at low AODs, and a decrease in COD with increasing AOD at higher AODs in accord with previous observational and modeling studies. The increase is attributed to a combination of microphysical and dynamical effects, whereas the decrease is attributed to a dominance of radiative effects that thin and darken clouds. An analogous relationship is shown for other modeled cloud variables as well. The similarity between the remotely sensed observations and model results suggests that these correlations are physically based and are not dominated by satellite retrieval artifacts. Cloud brightening due to BB is found to dominate in the early morning, whereas cloud inhibition is found to dominate in the afternoon and at night. BB decreased the net top of the atmosphere solar+IR irradiance modestly, but with large diurnal variation. We conclude that models that exclude treatment of aerosol radiative effects are likely to over-predict the microphysical effects of aerosols and underestimate the warming due to aerosols containing black and brown carbon.

Citation: Ten Hoeve, J. E., M. Z. Jacobson, and L. A. Remer (2012), Comparing results from a physical model with satellite and in situ observations to determine whether biomass burning aerosols over the Amazon brighten or burn off clouds, *J. Geophys. Res.*, 117, D08203, doi:10.1029/2011JD016856.

1. Introduction

[2] The effect of aerosols on clouds, precipitation, and the radiative balance remain one of the largest uncertainties in our climate system [Forster *et al.*, 2007]. Aerosols have been shown to influence clouds through microphysical effects, which increase cloud brightness [Twomey, 1977], lifetime [Albrecht, 1989], and vertical extent [Koren *et al.*, 2005] by increasing cloud droplet number concentrations [Andreae, 2009; Feingold *et al.*, 2001; Gunn and Phillips, 1957] and by decreasing low-level precipitation rates [Andreae *et al.*, 2004]. The reduction in warm precipitation due to microphysical effects has also been hypothesized to allow stronger updrafts to form, increasing cloud height and allowing additional latent heat of freezing to be released, in turn

increasing cloud ice, lightning, and convective precipitation [Andreae *et al.*, 2004; Khain *et al.*, 2005; Martins *et al.*, 2009; Rosenfeld and Woodley, 2000; Williams *et al.*, 2002].

[3] Aerosols have also been shown to influence clouds through radiative (semi-direct and cloud absorption) effects. The semi-direct effect arises as absorbing aerosol particles in the air warm the air relative to the surface, increasing the low-level atmospheric stability [Jacobson, 1998; Menon *et al.*, 2002]. An increase in stability reduces the vertical mixing of energy and moisture from the surface to the cloud, reducing the relative humidity in the cloud, thinning the cloud [Nicholls, 1984; Ramanathan *et al.*, 2005; Yu *et al.*, 2002; Zhang *et al.*, 2008]. The direct warming of the air around the cloud also reduces the relative humidity. The loss of cloud cover due to the increased stability and reduced relative humidity from absorbing aerosols below and around clouds is referred to as the semi-direct effect [Ackerman *et al.*, 2000; Hansen *et al.*, 1997; Jacobson, 2002a]. This effect is sensitive to the height of the aerosol layer relative to the cloud [Koch and Del Genio, 2010; Koren *et al.*, 2004; McFarquhar and Wang, 2006; Randles and Ramaswamy, 2008].

¹Department of Civil and Environmental Engineering, Stanford University, Stanford, California, USA.

²Laboratory for Atmospheres, NASA Goddard Space Flight Center, Greenbelt, Maryland, USA.

[4] The heating of a cloud due to the direct absorption of solar radiation by aerosol inclusions within cloud drops and interstitial aerosol particles between cloud drops is the cloud absorption effect. Black carbon (BC) within cloud drops warms the air more than it does outside of cloud drops due to multiple scattering of radiation inside cloud drops, increasing the likelihood that some of that radiation will intercept the BC [Grassl, 1975]. The cloud absorption effect has been used to explain in part why data indicate that thick clouds often have a low albedo [Danielson et al., 1969]. The effect has also been used to suggest through scaling arguments that the upper limit of the annual, global average of BC heating due to cloud absorption may be 1–3 W/m², dependent on the position of the BC in cloud drops [Chylek et al., 1996]. The effect has been modeled assuming a single BC inclusion within drops but not accounting for interstitial BC or multiple BC inclusions [Conant et al., 2002]. Global-scale calculations accounting for the absorption by multiple BC inclusions arising from nucleation scavenging and aerosol-hydrometeor coagulation, as well as absorption by BC interstitially between drops, suggest that interstitial and in-cloud absorption by BC may be a strong contributor to the global warming caused by BC [Jacobson, 2006, 2010].

[5] Observational and theoretical studies have suggested a smooth transition may exist among the competing microphysical and radiative aerosol effects on clouds [Koren et al., 2008; Rosenfeld et al., 2008; Ten Hoeve et al., 2011]. Over the Amazon, Koren et al. [2008] illustrated that microphysical effects appeared to dominate at low aerosol loadings, increasing cloud cover and height, whereas radiative effects appeared to dominate at higher aerosol loadings, decreasing cloud cover and height. Rosenfeld et al. [2008] also found an optimal aerosol optical depth (AOD) where convection is theoretically maximized at a similar AOD threshold to that found in Koren et al. [2008]. Observations of aerosol-cumulus cloud relationships over the Indian Ocean show a similar behavior [Dey et al., 2011]. A cloud-resolving modeling study of warm clouds over the Amazon Basin by Jiang and Feingold [2006] also showed this two regime behavior in cloud optical depth (COD) versus aerosol loading for simulations including radiative effects of aerosols on cloud heating and surface fluxes. Cloud fraction, liquid water path, cloud drop number, and surface latent and sensible heat flux all decrease in a simulation with radiative coupling compared to a simulation without radiative coupling [Jiang and Feingold, 2006].

[6] Many remote sensing studies have illustrated relationships between cloud properties and aerosol loading [Kaufman and Koren, 2006; Kaufman et al., 2005a; Koren et al., 2010a, 2008, 2005; Lin et al., 2006; Lindsey and Fromm, 2008; Loeb and Schuster, 2008; Quaas et al., 2008; Sekiguchi et al., 2003; Ten Hoeve et al., 2011; Yu et al., 2007]. However, these relationships may also be affected by other factors such as meteorological biases [Mauger and Norris, 2007; Ten Hoeve et al., 2011], swelling of aerosols near clouds [Myhre et al., 2007; Quaas et al., 2010; Twohy et al., 2009], or brightening of aerosols near clouds [Marshak et al., 2008; Várnai and Marshak, 2009; Wen et al., 2006]. Several studies have attempted to account for these confounding effects and conclude that observed correlations between aerosols and clouds are likely physically based [Jones et al., 2009;

Kaufman et al., 2005b; Koren et al., 2010a; Yuan et al., 2008]. Nevertheless, remotely sensed correlations between cloud properties and aerosol loading alone cannot determine causation [Stevens and Feingold, 2009]. Instead, coupling of remote sensing observations with 3-D simulations using a model that contains physical processes representing both microphysical and radiative effects is required to study more completely the impact of aerosols on clouds and climate. A few studies to date have compared remote sensing relationships between cloud variables and aerosol loading with modeled aerosol-cloud relationships [Myhre et al., 2007; Quaas et al., 2010, 2009]. Models used in these studies contained varying degrees of sophistication with respect to microphysical and radiative aerosol-cloud processes and also with respect to atmospheric feedbacks. Modeled aerosol-cloud relationships often did not resemble each other or the remotely sensed relationships, highlighting the need for continued research [Quaas et al., 2009].

[7] In this study, we perform high-resolution modeling simulations of both microphysical and radiative effects of biomass burning (BB) aerosols and gases on clouds, precipitation, and the regional radiative balance and compare modeled aerosol-cloud relationships with remotely sensed aerosol-cloud relationships. We then develop additional aerosol-cloud/precipitation/radiation relationships between simulations with (w/) and without (w/o) BB to isolate the effect of BB on the regional climate.

2. Methodology

2.1. Model Description

[8] GATOR-GCMOM is a one-way-nested Gas, Aerosol, Transport, Radiation, General Circulation, Mesoscale, and Ocean Model that simulates both weather and air pollution on global and regional scales. It is used and evaluated here to assess the short-term effects of BB aerosols on clouds and precipitation over the Amazon Basin. A similar modeling and data evaluation study analyzing urban pollution with GATOR-GCMOM over the Los Angeles Basin was conducted by Jacobson et al. [2007]. The model was described in detail by Jacobson [2010]. Global dynamics were solved with a mass-, energy-, vorticity-, and potential enstrophy-conserving scheme by Arakawa and Lamb [1981]. Regional dynamics were solved using finite difference solutions to the momentum, thermodynamic energy, and water continuity equations, as described by Jacobson [2001a]. A global domain and three nested regional domains were used. The grid resolution of the global domain was 4.0° NS × 5.0° WE and grid resolutions of the regional domains ranged between 1.0° NS × 1.0° WE for the coarsest domain and 0.2° NS × 0.2° WE for the finest domain (Figure 1). At these relatively coarse domain resolutions, cloud-scale thermodynamics and mesoscale circulations smaller than about five times the grid size could not be explicitly resolved. As a result, limitations existed with respect to simulating convection and cloud-scale microphysical-dynamical feedbacks in these model runs.

[9] Ground temperature and soil moisture in 10 subsurface layers in each subgrid surface class in each surface grid cell were computed online in the model. Each grid cell was divided into as many as 12 soil texture classes [Food and Agriculture Organization, 1996] and 15 surface classes according to Moderate Resolution Imaging Spectroradiometer

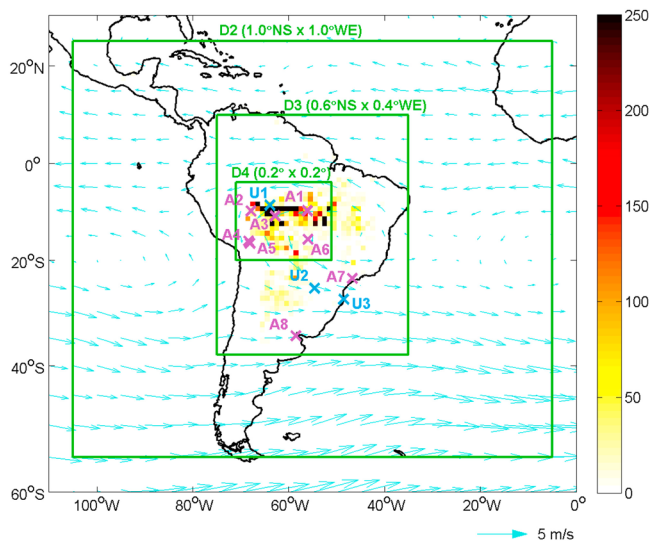


Figure 1. Locations and spatial resolutions of regional domains (D2–D4) employed in the 30-day simulation between 31 Aug 2006 and 30 Sep 2006. A global domain (D1) at $4.0^\circ \text{ NS} \times 5.0^\circ \text{ WE}$ resolution provides boundary conditions to D2. The color scale represents total GFEDv2 emissions (g/m^2) over the simulation. Vectors represent NCEP NCAR Reanalysis winds at 700 hPa. The locations of upper-air stations U1–U3 and AERONET stations A1–A8 used for model validation are also illustrated.

(MODIS) combined Terra/Aqua land cover data at 1 km resolution [Friedl *et al.*, 2010]. Rather than averaging soil parameters over each grid cell, a subgrid heterogeneous method was employed. Soil moisture and temperatures were tracked in each layer of each soil type in each grid cell, and fluxes determined at the surface of each soil type were averaged to obtain grid cell average fluxes [Jacobson, 2001a]. The land surface model and atmospheric model were coupled so that sensible and latent heat fluxes were calculated at each time step and in each grid cell based on properties of the subgrid land surface and the atmosphere, including impacts from clouds and aerosols. The vegetation fraction and leaf area index inside each soil class was determined each month from MODIS Terra Normalized Difference Vegetation Index (NDVI) data and MODIS Terra Leaf Area Index (LAI) data [Huete *et al.*, 2002; Wenzel *et al.*, 2006]. The Climate Prediction Center global monthly soil moisture data set was used to initialize soil moisture in the model [Fan and van den Dool, 2004].

[10] Gas processes treated include emissions, photochemistry, gas-to-particle conversion, gas-to-cloud conversion, gas-cloud exchange, gas-ocean exchange, convection, advection, molecular diffusion, turbulent diffusion, and dry deposition. Aerosol processes treated include emissions, homogeneous nucleation, condensation, dissolution, dry and wet deposition, aerosol-aerosol and aerosol-hydrometeor coagulation, sedimentation, and transport [Jacobson, 2002b]. Gases and particles were transported using a mass-conserving and peak-preserving advection scheme [Walcek, 2000]. An internally mixed aerosol size distribution with 14 size bins with diameters between 2 nm and $50 \mu\text{m}$, and three hydrometeor distributions (cloud/liquid, cloud/ice, and

cloud/graupel) each with 30 size bins with diameters between $0.5 \mu\text{m}$ and 8 mm, were used. Particle number and mole concentrations of 16 chemical species were tracked in each aerosol and hydrometeor size bin of each size distribution. Only one internally mixed aerosol distribution was used in these simulations since BB BC and organic carbon (OC) coagulate quickly after emission. A full list of the treated species is provided by Jacobson [2010, Table 1].

[11] Model simulations included a radiative transfer algorithm [Toon *et al.*, 1989] that determined diabatic heating rates, actinic fluxes for photolysis, and radiation available for photosynthesis [Jacobson, 2010]. A total of 694 wavelength intervals were used for radiative transfer through gases, aerosols, and cloud drops [Jacobson, 2005]. Wavelength-dependent optical properties of aerosols and clouds were calculated by integrating optical properties over each size bin in each aerosol and hydrometeor size distribution. Aerosol optical properties of some organic aerosol components used in the model are provided by Jacobson [1999]. For aerosol optical calculations, BC was treated as a core surrounded by a mixed shell. For cloud optical calculations, BC aggregates were treated as polydisperse spherules using the dynamic effective medium approximation [Jacobson, 2006]. Aerosol radiative effects were treated for aerosols in clear skies, aerosols within cloud and precipitation drops, and interstitial aerosols between cloud drops [Jacobson, 2010].

[12] The model treated the interaction of size- and composition-resolved aerosols with size- and composition-resolved mixed-phase clouds [Jacobson *et al.*, 2007]. Cumulus and stratus thermodynamics were determined with parameterizations; however, all cloud and precipitation microphysics were time-dependent, explicit, and size- and composition-resolved [Jacobson, 2003; 2010; Jacobson *et al.*, 2007]. Cloud thermodynamics were calculated with an Arakawa-Schubert cumulus parameterization that allowed the formation of between 0 and 500 subgrid cumulus clouds per column, each defined by a different cloud base and top. The parameterization was used to determine cumulus cloud fraction, cloud base and top heights, and cumulus redistribution of momentum to the grid scale [Ding and Randall, 1998]. Cumulus cloud fractions were calculated assuming no overlap, whereas combined cumulus-stratus cloud fractions were calculated assuming random overlap between individual layers.

[13] For each subgrid cloud, the model first calculated a vertical mass flux in each layer, which was used to determine rates of transport of moisture and energy to different levels in the cloud as well as the vertical extent of the cloud. The mass flux depended on the entrainment rate, stability, and moist static energy in the cloud. Grid-scale gases and size- and composition-resolved aerosol particles were then convected vertically among all layers of each subgrid cloud in a mass-conserving manner using a 1-D plume model [Jacobson, 2003]. Next, all bulk cloud and precipitation water in each layer in each subgrid cloud guessed by the cumulus parameterization was evaporated/sublimated and was allowed to recondense/redeposit on size- and composition-resolved aerosols in each vertical layer in a time-dependent manner based on Köhler theory, approximating aerosol activation during adiabatic ascent since the subgrid cumulus parameterization determined the moisture and energy transport to each layer in the cloud. In this way,

explicit aerosol-cloud microphysics were treated [Jacobson, 2003]. Microphysical processes accounted for in the model included condensation, evaporation, aerosol-hydrometeor and hydrometeor-hydrometeor coagulation, contact freezing by interstitial aerosols, heterogeneous and homogeneous freezing, drop breakup, sedimentation of hydrometeors and their aerosol inclusions, coagulation of precipitation hydrometeors with interstitial and below-cloud aerosols (wash-out), removal of precipitation and incorporated aerosols (rainout), below-cloud evaporation/sublimation to aerosol cores, gas washout, aqueous chemistry within liquid cloud and aerosol particles, and heterogeneous chemistry on ice crystals. When hydrometeor particles evaporated or sublimated, the aerosol core returned to the clear-sky aerosol size distribution. Ice crystals formed through heterogeneous nucleation and ice growth, evaporative freezing of liquid drops, contact freezing of liquid drops, and homogeneous plus heterogeneous freezing of liquid drops [Jacobson, 2003]. Temperature and water vapor changes due to microphysical calculations were added to the grid scale in an energy- and mass-conserving manner.

[14] In sum, the model physically treated both microphysical effects (changes to the number and sizes of cloud drops with resulting changes to cloud and precipitation characteristics) and radiative effects (semi-direct and cloud absorption effects) of black and brown carbon aerosols on mixed-phase clouds and precipitation. Aerosol microphysical effects on cloud ensembles were physically treated with an explicit size- and composition-resolved aerosol-cloud microphysics scheme [Jacobson, 2003; Jacobson *et al.*, 2007]. The model has the capability of simulating clouds explicitly, but for domain resolutions higher than the resolutions used in this study. Aerosol absorption effects were treated physically through wavelength-dependent aerosol absorption in clear skies, within cloud drops, and between cloud drops. Changes to the radiative balance were quantified through changes to the radiative flux at the surface and the top of the atmosphere (TOA), including feedbacks to meteorology [Jacobson, 2002a, 2010; Jacobson *et al.*, 2007].

2.2. Satellite Data Sets

[15] Daily Level 2 V5 AOD, COD, column water vapor, and cloud top pressure from the MODIS Aqua satellite were used to validate model results over the simulation period [Levy *et al.*, 2010; Platnick *et al.*, 2003; Remer *et al.*, 2005]. The 13:30 LT afternoon Aqua overpass was used instead of the 10:30 LT morning Terra overpass since cumulus clouds are more developed in the afternoon than the morning [Negri *et al.*, 2004]. The Level 2 MODIS data sets, at resolutions between 1 km and 10 km, were upscaled to the spatial resolution of the coarser model domains for comparison. MODIS AOD is retrieved for a wavelength of 0.55 μm and compares well with AEROSOL ROBOTIC NETWORK (AERONET) observations within an expected error envelope of $\pm(0.05 + 15\%)$ [Levy *et al.*, 2010]. Data that were considered “bad” according to the quality assurance data were removed. We also employed 3-h TRMM 3B42 precipitation rate data at $0.25^\circ \times 0.25^\circ$ resolution, also upscaled to the coarser resolution of the model domains, to validate daytime model precipitation rates [Huffman *et al.*, 2007; Kummerow *et al.*, 1998]. The 3B42 product combines high quality microwave

precipitation estimates with infrared precipitation estimates, scaled by rain gauge data [Huffman *et al.*, 2007].

2.3. In Situ Observations

[16] In situ observations of both aerosol and meteorological variables were paired with model results in time and space. Hourly surface observations of temperature, dew point, wind speed, and wind direction from the Integrated Surface Hourly Database (ISH) were used to validate surface model results over the simulation [Lott *et al.*, 2001]. A total of 347 stations were used for comparison throughout the study domain. Depending on the station, data were reported either hourly or 3 to 4 times per day. Modeled values were paired in time and space with each observation. Upper-air temperature, dew point, wind speed, and wind direction data from the Integrated Global Radiosonde Archive were used to validate upper-air meteorological variables averaged over the simulation [Durre *et al.*, 2006]. Model results at 35 levels were compared with radiosonde data at 14 pressure levels (1000, 925, 850, 700, 500, 400, 300, 250, 200, 150, 100, 70, 50, and 30 hPa). Radiosondes were released at 0Z and 12Z each day, and were compared with model values for those times. A total of 29 stations were located in our study domain during the study period; however, only a few representative stations are shown.

[17] Level 2.0 cloud-screened AOD measurements and single scattering albedo (SSA) inversions from up to eight AERONET stations were used to compare with model results [Holben *et al.*, 1998]. AERONET stations utilize ground-based sun-sky photometers to measure total aerosol loading and employ almucantar sky radiance scans to estimate aerosol properties in the cloud-free sky [Dubovik and King, 2000; Eck *et al.*, 1999]. Model results and AERONET observations were averaged over the simulation and were compared using tests of statistical significance. To retain only the most accurate retrievals, only AERONET inversions with a solar zenith angle greater than 50° , a sky-radiance fitting error less than 5.0%, and a sphericity greater than 90% were used. In addition, only SSA values (both measured and modeled) with a corresponding AOD above 0.5 were used to separate days dominated by BB emissions and days dominated by other aerosol sources such as urban aerosol.

2.4. Model Simulations

[18] The effect of BB on clouds and precipitation over the Amazon Basin was demonstrated through simulations that included and excluded BB emissions. BB particles can serve as cloud condensation nuclei [Andreae, 2009; Feingold *et al.*, 2001] but can also absorb visible and infrared radiation [Ramanathan *et al.*, 2005], thus participating in both microphysical and radiative effects. As these smoke particles age and are aggregated with other constituents, absorption is increased due to enhanced scattering into the BC core [Bond *et al.*, 2006; Jacobson, 2001c]. Fossil fuel, soil dust, and pollen/spore/bacteria aerosol, as well as biogenic emissions that convert to aerosol, were included in both simulations. Dry matter BB emissions were obtained from the Global Fire Emissions Database V2 (GFEDv2) assuming wood was 45% carbon by mass [van der Werf *et al.*, 2006]. In GFEDv2, emissions are produced at a spatial resolution of $1^\circ \times 1^\circ$ and at a temporal resolution of 8 days using MODIS 8-day fire

hot spots [Giglio *et al.*, 2003]. Dry matter emissions were classified by land cover type and were scaled by emission factors for both gases and particles according to the dominant land cover type [Andreae and Merlet, 2001; Defries and Townshend, 1994; Ferek *et al.*, 1998]. Particles emitted from BB emissions included BC, primary organic matter (POM), Na^+ , K^+ , Mg^{2+} , Ca^{2+} , NH_4^+ , $\text{H}_2\text{SO}_4(\text{aq})$, HSO_4^- , SO_4^{2-} , NO_3^- , and Cl^- . Coarse particle emissions were assumed to be 25% of fine mode BC emissions by mass and 45% of fine mode primary organic carbon (POC) emissions by mass [Jacobson, 2006]. The POM to POC ratio was assumed to be 2.1:1. The emissions were first fit to a continuous multimodal lognormal distribution according to measured distributions of fresh BB smoke [Janhäll *et al.*, 2010; Reid and Hobbs, 1998]. The continuous distribution was then discretized into size bins with BC particles assumed to consist of an aggregate of spherules coated by other chemical constituents such as POM [Jacobson, 2010]. Typical optical properties of BB aerosols in this region and season are provided by Dubovik *et al.* [2002]. The potential virtual air temperature inside each fire plume was assumed to be 5 K greater than the ambient air, in accordance with field measurements of wildfires in Brazil [Riggan *et al.*, 2004]. The emissions were then assumed to be well mixed to a height where the plume was buoyant (i.e., the potential virtual temperature equaled the ambient potential virtual temperature). Heat released from biomass combustion fed back to the temperature of the lowest layer at the grid scale. Water vapor emissions from BB were also included.

[19] Our study period extended from 12Z 31 Aug 2006 to 12Z 30 Sep 2006, during the peak of the BB season. BB is one of the primary sources of carbonaceous aerosols in the Southern Hemisphere [Seiler and Crutzen, 1980] and it dominates the regional aerosol loading during this season [Torres *et al.*, 2010]. Model simulations were initialized with $1^\circ \times 1^\circ$ reanalysis meteorological fields ($1^\circ \times 1^\circ$ reanalysis fields, 2006, Global Forecast System, <http://dss.ucar.edu/datasets/ds083.2/matrix.html>). Figure 1 illustrates the locations and spatial resolutions of the three regional domains utilized in the study (D2–D4). Forty-four vertical sigma-pressure levels were employed in the global domain and 35 levels were employed in the regional domains, with 15 layers in the bottom 1 km, 4 layers between 1 km and 3 km, 7 layers between 3 km and 10 km, and the remaining layers above 10 km. The thickness of the lowest model layer was 30 m. Also plotted in Figure 1 are GFEDv2 dry matter emissions summed over the 30-day study period in each $1^\circ \times 1^\circ$ grid box. Over domain D3, GFEDv2 reported total dry matter emissions of 215 Tg for the study period. Variables in higher resolution nested domains did not propagate to coarser domains due to the one-way nesting in the model. To study the causal effect of BB emissions in each domain, simulations including and excluding BB were run individually for domains D3 and D4. BB emissions were always included for domain D3 in simulations that included and excluded BB emissions for domain D4.

[20] Vectors in Figure 1 represent 700 hPa National Centers for Environmental Prediction (NCEP)/National Center for Atmospheric Research (NCAR) Reanalysis data averaged over the study period [Kalnay *et al.*, 1996]. Counterclockwise winds of the South American Subtropical High are visible in Figure 1 over eastern Brazil during this month

[Nobre *et al.*, 1998]. These winds advect BB emissions from source regions over the arc of deforestation to the southeast and eventually over the Atlantic Ocean. High pressure also minimizes the effect of meteorological variability on cloud properties, allowing aerosol effects to be better isolated in remotely sensed relationships [Koren *et al.*, 2004]. Patchy, shallow, non-precipitating cumulus clouds that form at the top of the boundary layer are most prevalent during this region and season [Nobre *et al.*, 1998]. Most convective clouds are constrained by large-scale subsidence within the aerosol layer; however, deep convective clouds, which may be decoupled from the smoke below, also occur at times. The majority of BB smoke exists at or below the cloud layer, although occasionally smoke plumes are pumped to higher altitudes through deeper cumulus convection. Cloud fields generally form by noon and dissipate overnight [Koren *et al.*, 2004; Negri *et al.*, 2004].

3. Results

3.1. Model Comparisons With Data

[21] We evaluated results from model simulations against satellite remote sensing observations, surface and upper-air meteorological measurements, and AERONET retrievals of aerosol properties. Figure 2 compares model results with remotely sensed observations of AOD, column water vapor, cloud-averaged COD, minimum cloud top pressure, and precipitation rate averaged over the 30-day simulation period for domain D3. Only model results corresponding to the daytime overpass times of MODIS and TRMM are used for comparison. We find consistency in the location and magnitude of the peak AOD between MODIS and model values in Figures 2a and 2b, yet the model under-predicts simulation- and domain-averaged AOD by 34%. This under-prediction of total AOD is common in tropical regions such as the Amazon, where heavy cloud cover and obscured surface burning due to the thick canopy can lead to large under-predictions of burned area used to estimate dry matter emissions [Giglio *et al.*, 2006]. Uncertainties in particle emission factors and other model processes may also contribute to the difference in aerosol loading. In Figures 2c and 2d, MODIS and model column water vapor are shown to compare quite well across the domain in both location and magnitude. Comparisons of MODIS and model cloud-averaged COD are shown in Figures 2e and 2f. Only cloudy-sky regions were included in the cloud-averaged COD to remove the influence of cloud fraction on the domain-averaged COD. Thus, no clear-sky values were included in the average. The model shows adequate skill at predicting the location of high and low COD regions, yet some areas in the southeast portion of the domain are under-predicted. The simulation- and domain-averaged COD also compares well. Figures 2g and 2h also show rather good agreement of minimum cloud top pressure (i.e., the average lowest pressure detected in each grid cell in each daily comparison) between MODIS and the model, with a slight under-prediction of cloud top pressure by the model over land and an over-prediction by the model over oceans. Standard deviations taken over all comparisons in time and space in Figures 2a–2h are also largely consistent between MODIS observations and model results.

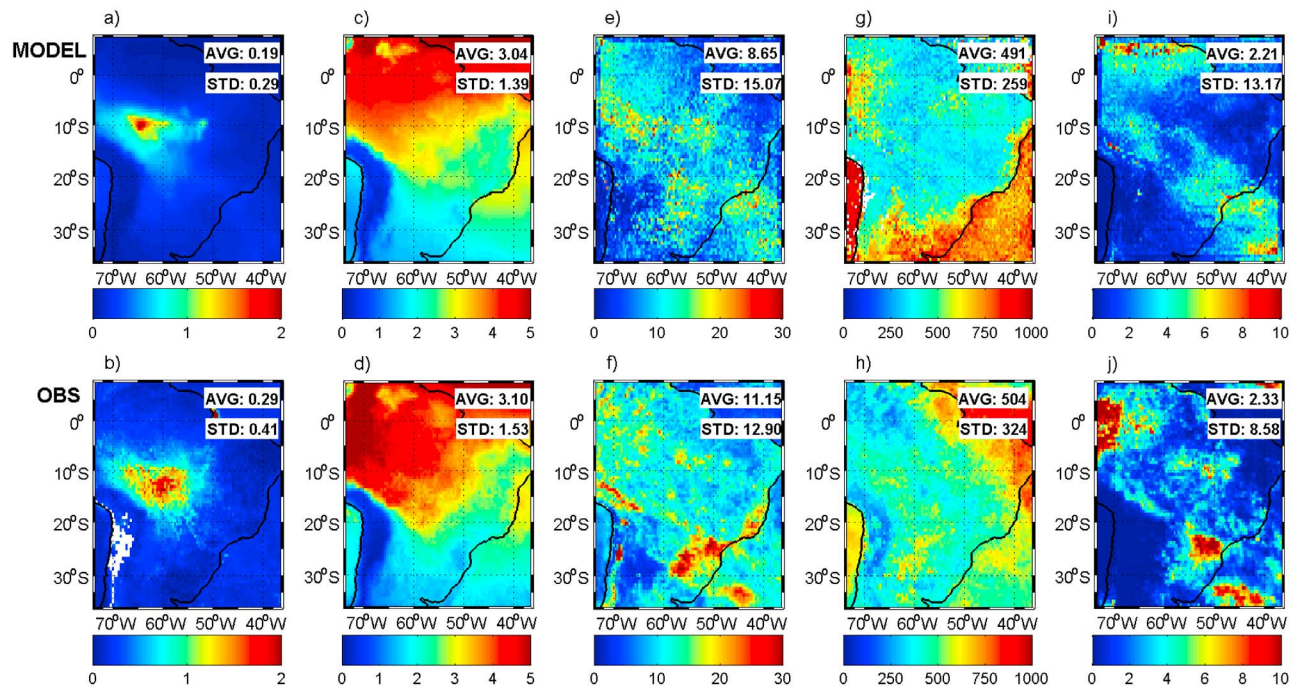


Figure 2. Comparisons between simulation-averaged (a) GATOR-GCMOM modeled column AOD at 0.55 μm and (b) MODIS Aqua AOD at 0.55 μm , (c) modeled column water vapor and (d) MODIS Aqua column water vapor, (e) modeled cloud-averaged COD at 0.55 μm and (f) MODIS Aqua cloud-averaged COD, (g) modeled minimum cloud top pressure (hPa) and (h) MODIS Aqua minimum cloud top pressure (hPa), and (i) modeled daytime (7:00–18:00 LT) precipitation rate (mm/day) and (j) TRMM daytime precipitation rate for concurrent model value and remote sensing observations in domain D3. Model values greater than the detectability threshold of the TRMM and MODIS sensors were excluded. Area-weighted averages (AVG) and standard deviations (STD) taken over all comparisons in time and space are noted in the inserts.

[22] Figures 2i and 2j show comparisons between TRMM daytime precipitation rate and model daytime precipitation rate. The model underestimates the magnitude of the highest precipitation areas and replicates the location of those areas only somewhat well. Because these model simulations did not resolve clouds explicitly, some difference between model values and observations in Figures 2e–2j is to be expected. Mesoscale circulations smaller than the grid scale, particularly those created by convective outflow, were not resolved. Furthermore, the microphysical-dynamical relationships between aerosols and clouds on the individual cloud scale were not resolved in time, contributing to the difference between observations and model results [Khain *et al.*, 2005]. The model does, however, match the simulation- and domain-averaged precipitation well in Figures 2i and 2j with an average precipitation rate only 5% below the observed rate. Yet, this agreement could also be attributed to constraints on the regional hydrological budget. Auxiliary material Figure S1a shows the distribution of clouds modeled in the study for domain D4.¹ The majority of clouds (>70%) formed in the simulation are shallow clouds with CODs below 10. Auxiliary material Figure S1b indicates that as COD increases, average precipitation in the grid cell

also increases as expected, but auxiliary material Figure S1c indicates that the total amount of precipitation over the simulation is at a maximum for CODs near 40. This is the optimal value given that the majority of clouds are small clouds but the average precipitation is higher for large clouds. Overall, only a small fraction of the total precipitation over the simulation falls from the most common shallow cumulus clouds.

[23] Figure 3 shows comparisons of temperature, dew point, wind speed, and wind direction averaged over the 30-day simulation for three representative upper-air stations in domains D3 and D4 to validate model skill of non-surface meteorological variables. Station locations are illustrated in Figure 1. Station U1 is located within the heaviest BB region, station U2 is located downwind of the heaviest burning region, and station U3 is located near the coast, farthest downwind of the region of heaviest burning. In Figures 3a, 3c, and 3e, temperature and dew point are modeled well for all three locations. Dew point is slightly over-predicted in the mid-troposphere below 700 hPa for station U2 and station U3, yet differences between observations and model values are rather small when taking into account the standard error at these pressure levels. In Figures 3b, 3d, and 3f, wind speed and wind direction match very well at stations U2 and U3, with some inconsistencies at station U1. The shape of the wind speed and wind

¹Auxiliary materials are available in the HTML. doi:10.1029/2011JD016856.

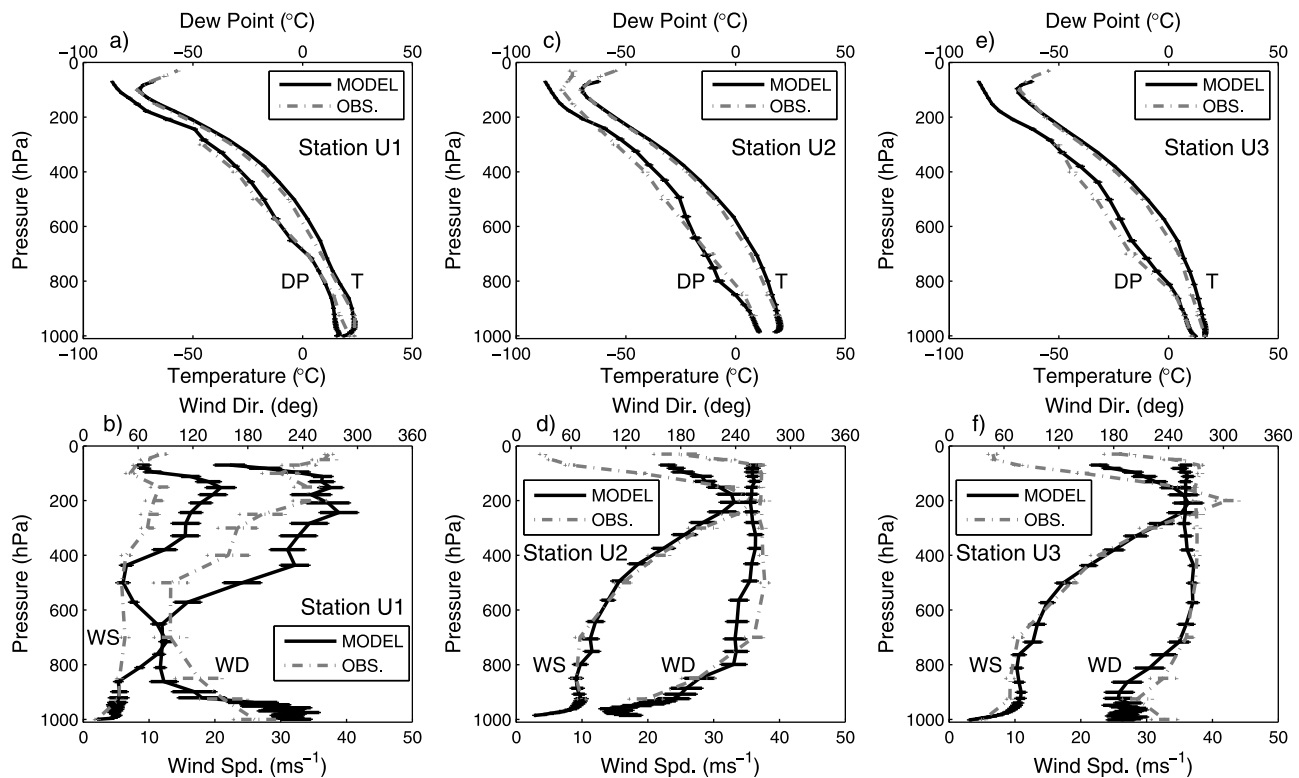


Figure 3. Comparisons between simulation-averaged temperature (T), dew point (DP), wind speed (WS), and wind direction (WD) for three representative upper-air stations in domains D3 and D4 over the 30-day simulation period. Observations are paired in time and space with model results over the simulation and are then averaged over all comparisons for each vertical level. Solid lines indicate model values and dashed lines indicate measured values. (a, c, and e) T and DP and (b, d, and f) WS and WD for each station. Station U1 (Figures 3a and 3b) is located in the region of heaviest biomass burning (8.70°S, 63.90°W), station U2 (Figures 3c and 3d) is located downwind of the biomass burning region (25.52°S, 54.58°W), and station U3 (Figures 3e and 3f) is located near the coast farthest downwind of the biomass burning region (27.67°S, 48.55°W). Station locations are pictured in Figure 1. For each station, model results from the highest resolution domain containing that station are employed. Horizontal bars at each pressure level indicate the standard error of the mean value at that pressure level.

direction profiles with height matches well between observations and model values, even if absolute values are somewhat higher in the model at station U1. In general, standard error bars overlap for the majority of the observations, indicating that differences between modeled and observed values are not statistically significant and that the model is predicting these variables with adequate skill.

[24] The skill at which traditional surface meteorological fields are predicted by atmospheric models can be judged with the following criterion: (1) $\sigma_m \sim \sigma_{obs}$ (2) $E < \sigma_{obs}$ and (3) $E_{UB} < \sigma_{obs}$ where σ is the standard deviation, E is the root mean square error (RMSE), and E_{UB} is the bias-corrected RMSE [Keyser and Anthes, 1977; Pielke, 2002]. The subscript m refers to the model results and the subscript obs refers to the data. Table 1 shows statistics for four surface meteorological fields over all surface ISH stations and observations used for comparison. These statistics are computed across all stations and observations over the 30-day simulation. Table 1 indicates that criteria (1), (2), and (3) are met for temperature, dew point, and wind direction. Criteria (2) and (3) do not pass for wind speed, yet the standard deviations match rather well, meeting criterion (1).

In addition, mean bias and mean normalized bias are rather low for all variables, including wind speed. Overall, the model predicts the surface temperature, dew point, and wind direction very well, and predicts the wind speed acceptably well over our simulation region and period.

[25] Figure 4a compares column AERONET AOD measurements and model-predicted column AOD averaged over the simulation for eight AERONET stations across South America in domains D3 and D4. Station locations are pictured in Figure 1. Observations are paired with model results in time and space, and are then averaged to an 8-day temporal resolution matching the temporal resolution of the GFEDv2 input data set. The model compares well with AERONET measurements in all areas: in BB source regions (A1–A3), in sites along the Andes (A4–A5) and in regions downwind of BB (A6–A8). We find that the average AOD in BB source regions is over-predicted by the model at stations A2 and A3 but is slightly under-predicted at A1 compared to AERONET observations. The difference in mean values between AERONET and the model fail a non-directional t-test for statistical significance at the 90% confidence interval for all stations, indicating statistical similarity

Table 1. Comparison of Model Results With ISH Meteorological Observations of Temperature, Dew Point, Wind Speed, and Wind Direction Paired in Time and Space Over the 30-Day Simulation Period for Stations Within Domains D3 and D4^a

	Temperature (K)		Dew Point (K)		Wind Speed (ms ⁻¹)		Wind Direction (deg)	
	Obs.	Model	Obs.	Model	Obs.	Model	Obs.	Model
Mean Value	21.0	21.3	12.7	9.5	4.0	3.0	186.3	196.5
Standard Deviation (σ)	7.8	9.7	8.4	7.3	2.2	1.7	139.0	106.2
Mean Bias		0.25		−3.2		−1.0		5.5
Normalized Bias (%)		0.097		−1.08		−5.77		1.54
RMSE (E)		7.2		6.8		2.9		113.1
Bias-Corrected RMSE (E _{ub})		7.2		6.0		2.7		112.9
Number of Stations		347		347		342		344
Number of Comparisons		86512		86512		63909		71407

^aFor each station, model results from the highest resolution domain containing that station were employed. Mean values, standard deviations, mean bias (model – obs), mean normalized bias 100*[(model – obs)/obs], RMSE, bias-corrected RMSE, and the number of observations and stations are reported. Statistics were computed over all stations and observations. Wind speed observations below 1.5 were excluded.

between the model and data for all stations. Additionally, the normalized bias over all stations and observations is low (+16%) as the model over-predicts AOD at four sites and under-predicts AOD at four sites.

[26] Figure 4b illustrates comparisons between simulation- and domain-averaged AERONET inversions of SSA and modeled SSA for six of the eight AERONET stations with aerosol inversions in Figure 4a. Spectrally resolved SSA in each grid cell and at each time step was predicted from size- and composition-resolved aerosols in the model, and was averaged to an 8-day temporal domain similar to Figure 4a. We find rather good comparisons between modeled SSA and inverted SSA from AERONET measurements, as well as between modeled SSA and previous studies [Dubovik *et al.*, 2002; Eck *et al.*, 2003; Remer *et al.*, 1998]. For stations in BB source regions, we find a slight under-prediction of the SSA by ~ 0.03 at stations A1 and A3, located in the southeast and south central Amazon, respectively, and an over-prediction of the SSA by ~ 0.06 at station A2, located in the southwest Amazon. In stations farther to the southeast, we find a slight over-prediction of the SSA. The difference in mean values between AERONET and the model fail a non-directional t-test for statistical significance at the 90% confidence interval for only one station, yet, significance could not be determined at stations A7 and A8 due to a lack of sufficient data. However, the model yields a low total normalized bias over all stations and observations (+0.11%). BB in the arc of deforestation is dominated by forest fires whereas regions to the southeast of the arc of deforestation are largely dominated by savanna and agricultural fires [van der Werf *et al.*, 2010]. The physical and optical properties of aerosols derived from forest and savanna fires in the Amazon are markedly different [Eck *et al.*, 2003; Remer *et al.*, 1998]. In particular, savanna grass and agricultural residue have a higher combustion efficiency and produce relatively higher amounts of BC compared to woody-fuel forest fires, resulting in a lower SSA of the emitted aerosol [Ward *et al.*, 1992]. We find that just downwind of the heart of Brazilian agricultural sugarcane production, station A7 (São Paulo) exhibits lower modeled SSA and AERONET SSA than stations within the Amazon Basin, as expected. This lower SSA may also partially result from darker urban aerosol which may have also been present during days dominated by BB aerosol.

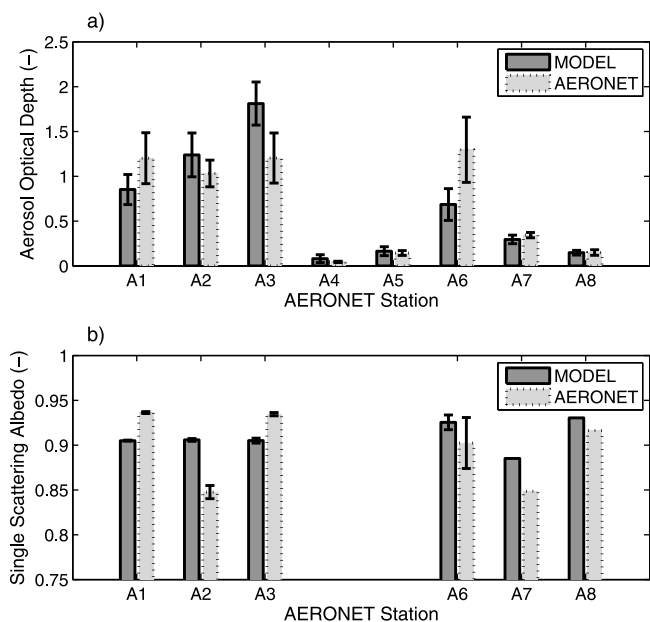


Figure 4. (a) Comparison of simulation-averaged column clear-sky aerosol optical depth at $0.440 \mu\text{m}$ between AERONET measurements and model results over the eight AERONET stations, pictured in Figure 1. Error bars represent the standard error of the average value. For each station, model results from the highest resolution domain containing that station were employed. Station A1 corresponds to Alta Floresta (9.87°S , 56.10°W , 200 m), A2 corresponds to Rio Branco (9.96°S , 67.87°W , 212 m), A3 corresponds to Ji Paraná SE (10.93°S , 62.85°W , 218 m), A4 corresponds to Mount Chacaltaya (16.35°S , 68.13°W , 5233 m), A5 corresponds to La Paz (16.54°S , 68.07°W , 3439 m), A6 corresponds to Cuiabá-Miranda (15.73°S , 56.02°W , 210 m), A7 corresponds to São Paulo (23.56°S , 46.73°W , 865 m), and A8 corresponds to Ceilap-BA (34.57°S , 58.50°W , 10 m). (b) Comparison of simulation-averaged column clear-sky SSA at $0.675 \mu\text{m}$ between AERONET inversions and model values for the six AERONET stations containing SSA inversions during the simulation period. Error bars, representing the standard error of the average values, could not be calculated for stations A7 and A8 due to a lack of sufficient AERONET data.

Table 2. Modeled Area-Weighted Simulation- and Domain-Averaged Values w/ BB and Percent Differences Between Simulations w/ BB and w/o BB for Domains D3 and D4^a

Variable	w/ BB (Domain D3)	Percent Diff. w/– w/o BB (Domain D3) (%)	w/ BB (Domain D4)	Percent Diff. w/– w/o BB (Domain D4) (%)
Column aerosol mass (g/m ²)	0.0569	+66.1	0.153	+114.4
Column aerosol number (#/cm ²)	$3.39 \times 10^{+9}$	+2.62	$3.77 \times 10^{+9}$	+14.7
Column AOD at 0.55 μm (–)	0.191	+120.6	0.633	+159.6
Column aerosol absorption optical depth at 0.55 μm (–)	0.0269	+285.0	0.113	+285.0
Clear-sky column SSA at 0.55 μm (–)	0.905	–2.27	0.857	–4.05
Surface net solar irradiance (W/m ²)	235.1	–3.57	215.2	–11.6
Surface net IR irradiance (W/m ²)	–107.1	+2.55	–105.0	+8.93
Surface net solar+IR irradiance (W/m ²)	128.0	–4.42	110.2	–14.1
Near-surface air temperature (°C)	21.8	–1.38	23.3	–3.41
TKE (m ² /s ²)	0.395	–1.55	0.365	–6.30
Sensible heat flux (W/m ²)	35.0	–7.27	31.1	–21.3
Latent heat flux (W/m ²)	73.8	–1.94	43.9	–4.84
Soil moisture (m ³ /m ³)	0.129	+5.50	0.113	+21.6
Column water vapor (g/m ²)	$3.05 \times 10^{+4}$	–0.159	$3.23 \times 10^{+4}$	+1.44
Cloud-averaged COD (–)	13.8	+27.0	15.1	+43.3
Cloud-averaged cloud absorption optical depth (–)	2.93×10^{-4}	+202.9	7.19×10^{-4}	+253.8
Column cloud liquid drop number (#/cm ²)	$8.08 \times 10^{+5}$	+72.5	$5.59 \times 10^{+5}$	+220.9
Column cloud ice crystal number (#/cm ²)	$2.80 \times 10^{+4}$	–7.73	$1.13 \times 10^{+4}$	+18.6
Ratio column drop number to total CCN (–)	0.0148	+50.8	0.0111	+122.1
Ratio column crystal number to total IDN (–)	5.75×10^{-4}	–4.06	4.26×10^{-4}	+10.8
Column cloud liquid (g/m ²)	19.2	+2.32	11.7	+15.2
Column cloud ice (g/m ²)	5.07	–7.10	4.13	+21.0
Ratio of column cloud liquid to cloud ice (–)	3.78	+10.1	2.84	–4.82
Cloud fraction (–)	0.244	–2.93	0.110	+1.19
Precipitation (mm/day)	1.92	–1.26	1.09	+9.43
Lightning (flashes/km ² -yr)	3.94	–8.75	5.01	+27.7
Minimum cloud top pressure (hPa)	448.4	+0.209	404.4	+1.34
Geometric mean number diameter of liquid drops (μm)	11.1	–21.36	7.30	–46.02

^aPercent differences are relative to simulations w/o BB. All column amounts include both anthropogenic and natural contributions. Only 3 to 4 significant digits are shown.

3.2. Aerosol-Cloud Relationships Determined From Simulations w/ BB Minus Simulations w/o BB and Remote Sensing Observations

[27] The effect of BB on clouds, precipitation, and the radiative balance of the atmosphere is studied through simulations that included and excluded BB emissions. Table 2 shows area-weighted simulation- and domain-averaged differences between simulations w/ BB and w/o BB in domains D3 and D4. Averaged column aerosol number, mass, optical depth, and absorption optical depth increase in the simulation w/ BB relative to the simulation w/o BB for both domains. The addition of BB aerosols and gases decreases surface net downward solar irradiance due to (1) backscattering and absorption of incoming solar radiation [Ackerman *et al.*, 2000] and (2) microphysical aerosol effects which increase cloud brightness [Coakley *et al.*, 1983; Twomey, 1977]. Surface net downward infrared irradiance increases as BB aerosols and gases scatter and absorb radiation [Jacobson, 1998, 2001b]. Even though the majority of BB aerosols are smaller than the wavelength of infrared energy, some aerosol is emitted to the coarse mode, fine mode aerosol coagulates to the coarse mode, and aerosols grow to larger sizes. IR extinction may be attributed to these larger aerosols, as well as from BB gases such as H₂O, O₃, and CO₂. A similar change in thermal IR (~+10–15%) at the surface has been shown in multiple studies for regions of urban pollution without feedbacks to clouds [Bergstrom and Viskanta, 1973; Jacobson, 1997]. Here, changes to cloud cover and the thermal structure of the

atmosphere between simulations w/ BB and w/o BB also contribute to the change in the surface IR. The surface net downward solar+IR irradiance averaged over the simulation is negative, indicating an overall cooling of the earth's surface. A corresponding decrease in the simulation and domain-averaged surface air temperature is detected in both domains D3 and D4, with a decrease in turbulent kinetic energy (TKE) corresponding to a stabilization of the lower boundary layer [Yu *et al.*, 2002].

[28] Figure 5a shows time-averaged vertical profiles of temperature and TKE for the simulation w/ BB minus w/o BB for domain D4. Temperatures increase in the simulation w/ BB at the aerosol layer near 800 hPa as a result of absorption by BC and brown carbon in BB aerosols [Feingold *et al.*, 2005]. This height corresponds rather well with direct observations of the aerosol layer height in the region [Davidi *et al.*, 2009]. A decrease in temperature is also detected at the surface, stabilizing the lower boundary layer. This surface cooling and lower-tropospheric warming results in a large area of regional subsidence, the formation of a surface thermal high pressure, and surface divergence of air between simulations w/ BB and w/o BB (auxiliary material Figure S2). The magnitude of the surface pressure increase due to BB is similar to that provided by Zhang *et al.* [2009].

[29] Stabilization of the lower boundary layer is further evidenced by the decrease in TKE below the aerosol layer in Figure 5a, which in turn reduces surface fluxes of sensible

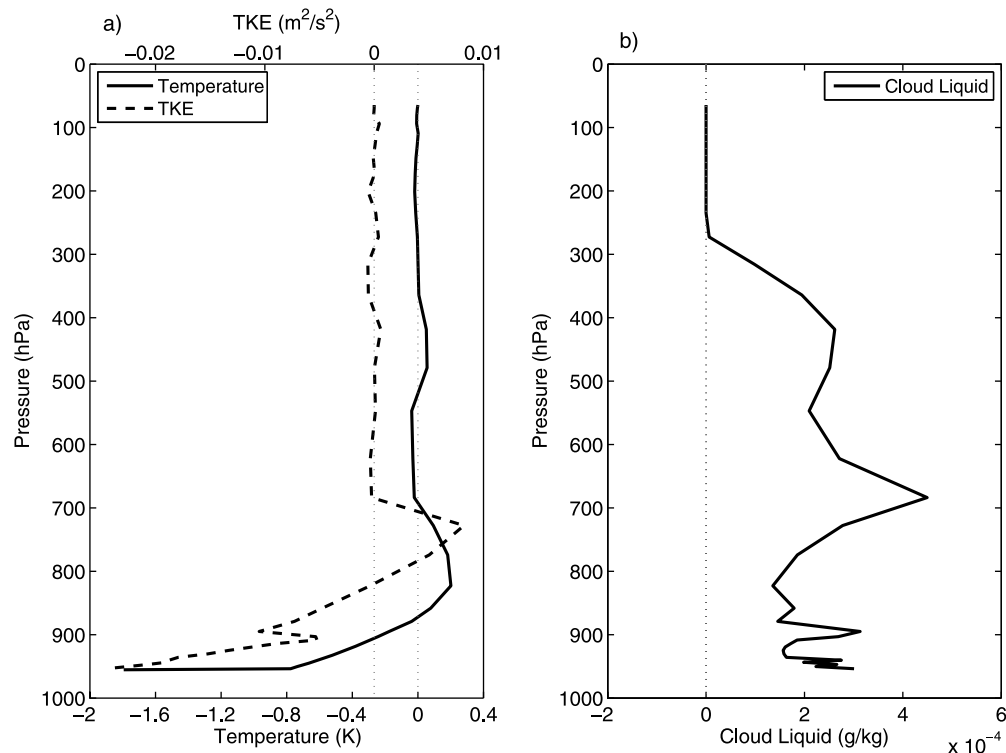


Figure 5. Vertical profiles of (a) temperature (K) and TKE (m^2/s^2) and (b) cloud liquid water (g/kg-dry air) for the simulation w/ BB minus the simulation w/o BB in domain D4. All values are time-averaged over the simulation.

and latent heat [Jacobson, 1998; Jiang and Feingold, 2006; Yu *et al.*, 2002], as indicated in Table 2. The reduction in latent heat flux in the simulation w/ BB is only $\sim 25\%$ of the reduction in sensible heat flux (Table 2), which agrees with a study by Zhang *et al.* [2008] over the Amazon. This decrease in latent heat flux also serves to increase surface soil moisture in the simulation w/ BB (Table 2). The contribution of increased surface water vapor flux from BB combustion between the simulations w/ and w/o BB is found to be relatively small, at a rate of 0.000868 mm/day averaged over domain D4, which equates to 0.056% of the average evapotranspiration rate (1.55 mm/day) and 0.080% of the average precipitation rate (1.09 mm/day), yet localized effects may be more substantial. The increase in temperature at the aerosol layer serves to destabilize the atmosphere directly above the aerosol layer, as also indicated by the increase in TKE [Feingold *et al.*, 2005; Koch and Del Genio, 2010]. Figure 5b shows the difference in cloud liquid water between the simulations w/ and w/o BB. The largest increase in cloud liquid water exists directly above the aerosol layer at a similar height to the increase in TKE in Figure 5a, suggesting that destabilization of the atmosphere above the aerosol layer by aerosol absorption may play a role in cloud formation. In addition, this peak in cloud liquid water only exists in the ~ 150 hPa above the aerosol layer, suggesting that the vertical extent of convection due to destabilization is limited to a shallow layer.

[30] Simulation and domain-averaged COD is 27% and 43% higher in the simulation w/ BB in domains D3 and D4, respectively (Table 2). Cloud absorption optical depth is also higher as a result of the optically thicker clouds. However,

we also find that COD does not increase monotonically with increased BB aerosol loading. Figure 6 shows both MODIS Aqua cloud-averaged COD and model cloud-averaged COD in the simulation w/ BB binned by MODIS and model AOD, respectively, for domain D4. AODs are restricted to below 0.9 to allow for the analysis of aerosol effects at relatively high AODs, but also to prevent aerosol misclassification as cloud [Brennan *et al.*, 2005]. Four bins of equal width are employed between AODs of 0.01 and 0.2 to resolve aerosol effects at low AODs, and seven bins of equal width are employed between AODs of 0.2 and 0.9 . Cloud contamination of aerosol may still occur in this range, but significant contamination is unlikely [Kaufman *et al.*, 2005b]. Remotely sensed AOD is only possible in clear-sky regions, yet we assume the clear-sky AOD is equal to the cloudy-sky AOD in each grid box. Only cloudy regions are included in the cloud-averaged COD; therefore, situations where meteorological conditions result in cloud-free skies with high AOD are not included. Error bars denote the standard error of the mean value in each bin.

[31] Figure 6a shows that both MODIS and model cloud-averaged COD increase with increasing AOD to an AOD of ~ 0.3 , and then decrease with increasing AOD between ~ 0.3 and 0.9 . A similar relationship has been found in observational studies of aerosol-cloud correlations over the Amazon [Koren *et al.*, 2008; Ten Hoeve *et al.*, 2011], in cloud-resolving large eddy simulations of warm clouds over the Amazon [Jiang and Feingold, 2006], and is consistent with theory [Rosenfeld *et al.*, 2008]. The increasing followed by decreasing relationship is attributed to competing microphysical and radiative effects of aerosols. The increase in

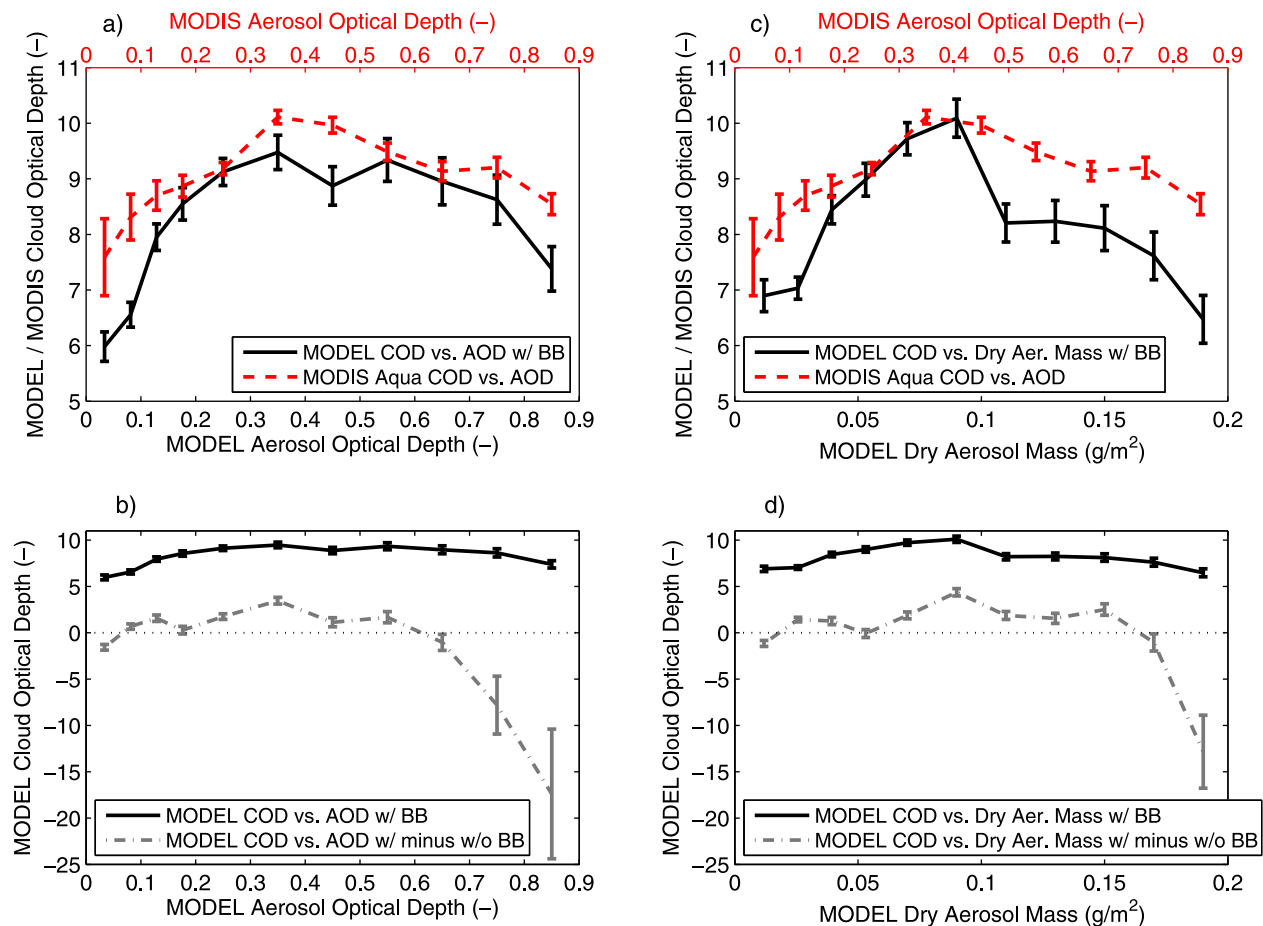


Figure 6. (a) Model cloud-averaged COD at $0.55 \mu\text{m}$ and MODIS Aqua cloud-averaged COD binned by model and MODIS AOD at $0.55 \mu\text{m}$ for all grid cells in domain D4. MODIS observations are averaged to the spatial resolution of domain D4. Only times corresponding to an Aqua overpass and only values within the detection range of the sensor are included in the model results. Error bars represent the standard error of the mean value in each bin. (b) Model cloud-averaged COD binned by AOD identical to Figure 6a (but with a different y axis scale) and cloud-averaged COD binned by AOD differenced between simulations w/ BB and w/o BB. COD values are differenced for each AOD bin. Error bars represent the square root of the sum of the squared errors of the simulations w/and w/o BB. (c) Same as Figure 6a but for cloud-averaged COD binned by dry aerosol mass for the same model times and locations used in Figure 6a (g/m^2). (d) Same as Figure 6b but for cloud-averaged COD binned by dry aerosol mass for the same model times and locations used in Figure 6b (g/m^2).

COD at low AODs is due to a combination of more numerous cloud drops with a lower mean drop radius (Table 2 and Figure 7a) and higher cloud liquid water (as shown in Figure 7c). At higher AODs, microphysical effects saturate due to the limited availability of liquid water [Kaufman and Fraser, 1997], whereas radiative effects of aerosols outside, within, and between cloud drops, which serve to thin and darken clouds as well as reduce surface heat and moisture fluxes, increase in magnitude.

[32] Since both MODIS and the model follow a similar increasing then decreasing relationship, we suggest that this relationship has a physical basis and is not dominated by MODIS retrieval artifacts such as brightening of aerosols near clouds [Wen et al., 2006], cloud contamination of aerosol, or artificial reduction of CODs under a lofted absorbing aerosol layer [Wilcox et al., 2009], even though these artifacts may still be present. This relationship is also

not likely dominated by increased humidity near clouds, which can increase aerosol scattering [Twohy et al., 2009], since a similar increasing followed by decreasing relationship is shown for cloud-averaged COD binned by dry aerosol mass substituted for AOD (Figure 6c).

[33] Figure 6a illustrates the correlation between cloud-averaged COD and AOD. Variability in the background meteorology, not associated with BB aerosols, may also play a role in the relationship [Ten Hoeve et al., 2011]. To analyze the causal effect of BB, differences between simulations w/ BB and w/o BB were studied. Figure 6b shows cloud-averaged COD binned by AOD for the simulation w/ BB, similar to Figure 6a but plotted on a different y axis scale, as well as the difference in cloud-averaged COD binned by AOD between simulations w/ BB and w/o BB. The dashed line representing the differenced simulation illustrates the causal effect of the BB aerosols relative to the simulation

with only background aerosol. The difference in COD is positive for AODs from ~ 0.1 – 0.6 . BB aerosols are generally smaller relative to background aerosols (82% of aerosol mass is contained in aerosol sizes below $2.5 \mu\text{m}$ in the simulation w/ BB compared with 75% in the simulation w/o BB). As a result, for the same AOD loading in the simulation w/ BB minus w/o BB, there are more cloud condensation nuclei (CCN) in the simulation w/ BB than the simulation w/o BB for AODs between ~ 0.1 and 0.6 (as shown in Figure 7a). The higher CCN concentration in the simulation w/ BB results in more cloud drops that grow to smaller sizes. This serves to increase the COD in the simulation w/ BB relative to the simulation w/o BB for the same cloud water content. At AODs below ~ 0.1 , COD is slightly higher for the simulation w/o BB. At these very low AODs, the simulation w/ BB contains a larger fraction of small particles that activate less readily relative to the simulation w/o BB for the same AOD, in turn resulting in a lower COD in the simulation w/ BB. At AODs higher than ~ 0.1 , there is a greater number of large and small particles and so the simulation w/ BB contains more CCN that can activate relative to the simulation w/o BB.

[34] In Figure 6a, the AOD value of ~ 0.3 at which the slope of the MODIS and model curves change from positive to negative represents the AOD threshold at which radiative effects exceed microphysical effects in the simulation w/ BB, and COD begins to decrease with increasing AOD. This AOD threshold is consistent with the threshold provided by *Koren et al.* [2008]. The AOD value of ~ 0.6 in Figure 6b at which the w/ BB minus w/o BB curve changes from positive to negative represents the AOD threshold at which clouds become optically thinner in the simulation w/ BB compared to w/o BB. Because the simulation w/ BB exhibits a generally stronger microphysical effect at low AODs and a stronger radiative effect at higher AODs than the simulation w/o BB, the AOD threshold at which the w/ BB minus w/o BB curve changes from positive to negative in Figure 6b is higher than the AOD threshold at which radiative effects begin to dominate microphysical effects in the simulation w/ BB in Figure 6a. Therefore, clouds are optically thicker at AODs between ~ 0.1 and ~ 0.6 and are optically thinner at AODs higher than ~ 0.6 in the simulation w/ BB compared to the simulation w/o BB, even though the AOD threshold at which dominance of microphysical effects gives way to dominance of radiative effects in the simulation w/ BB occurs at a lower AOD.

[35] At AODs between ~ 0.6 and 0.9 , the COD becomes negative in the simulation w/ BB relative to the simulation w/o BB. At these higher AODs, radiative effects of absorbing BB aerosols, which reduce surface fluxes and burn off clouds at the aerosol layer [*Feingold et al.*, 2005; *Yu et al.*, 2002], thin clouds in the simulation w/ BB compared to w/o BB. Locally high AODs in the simulation w/o BB are from pollen/spore/bacteria aerosols, soil dust aerosols, and biogenic organic gases that convert to particles, many of which have also hygroscopically grown in humid environments, but are not as absorbing as BB aerosols. This radiative effect at high AODs also suggests that destabilization above the aerosol layer (Figure 5) does not fully account for changes in COD between the simulations or further increases in COD would likely be observed at high AODs. Significantly fewer COD-AOD pairs exist for the

simulation w/o BB compared with the simulation w/ BB at high AODs (auxiliary material Table S1), resulting in the larger error bars at higher AODs. Figure 6d shows a similar result to Figure 6b with cloud-averaged COD binned by dry aerosol mass instead of AOD, again suggesting that these relationships are not dominated by the effect of humidification of aerosols near clouds. The number of COD-AOD pairs for dry aerosol mass in Figures 6c and 6d is given in auxiliary material Table S2.

[36] Simulation- and domain-averaged cloud fraction, precipitation, column cloud liquid drop number, column cloud ice crystal number, column cloud liquid water, and column cloud ice increase in the simulation w/ BB in domain D4 (Table 2). Increases in column cloud liquid drop number and cloud liquid water are consistent with aerosol microphysical effects which grow more activated CCN to smaller sizes and enhance cloud development [*Quaas et al.*, 2008]. The increase in column cloud ice crystal number and cloud ice also suggest an invigoration of cold cloud processes. The greater number of ice crystals (due to BB particles serving as ice deposition nuclei) and increased cloud ice also result in a +28% increase in lightning flashes in domain D4. The ratio of cloud liquid to cloud ice in domain D4 decreases by 4.8% as increases in cloud ice outpace increases in cloud liquid. Yet, the ratio of cloud liquid to ice remains high as shallow liquid cumulus clouds still dominate the cloud field (auxiliary material Figure S1). In domain D3, cloud fraction, precipitation, column cloud ice crystal number, and column cloud ice decrease in the simulation w/ BB compared with the simulation w/o BB due to a slowing of the larger regional hydrological cycle by BB aerosols [*Ramanathan et al.*, 2005]. However, similar to COD in Figure 6, we find that many of these cloud variables are influenced by competing aerosol effects at different degrees of aerosol loading, discussed below.

[37] Figure 7 shows several model variables binned by AOD for daytime hours of the simulation w/ BB (black lines) and for the simulation w/ BB minus w/o BB (gray lines) in domain D4. Figure 7a shows that column cloud liquid drop number generally increases with AOD in the simulation w/ BB along the range of AODs studied, with a lower rate of increase at AODs above ~ 0.15 due to saturation effects. However, column cloud ice crystal number (Figure 7b), column cloud liquid water (Figure 7c), cloud fraction (Figure 7d), and precipitation rate (Figure 7e), exhibit a decrease with increasing AOD for AODs above ~ 0.1 in the simulation w/ BB. This threshold of ~ 0.1 between increasing and decreasing cloud fraction in Figure 7d is at a slightly lower AOD than the threshold in Figure 6a or the threshold observed by *Koren et al.* [2008], but is consistent with a study by *Myhre et al.* [2007] that suggests increases in cloud fraction below AODs of ~ 0.2 may be due to aerosol microphysical effects, but increases in cloud fraction above AODs of ~ 0.2 may be due to other non-aerosol effects such as meteorological variation. For instance, low cloud fractions at high AODs may be explained by the fact that high pressure favors both high AOD conditions as well as cloud-free skies. The exact AOD threshold separating the dominance of aerosol microphysical and radiative effects in the simulation w/ BB may also be somewhat uncertain. The decreasing behavior with increasing AOD in the simulation w/ BB agrees with some

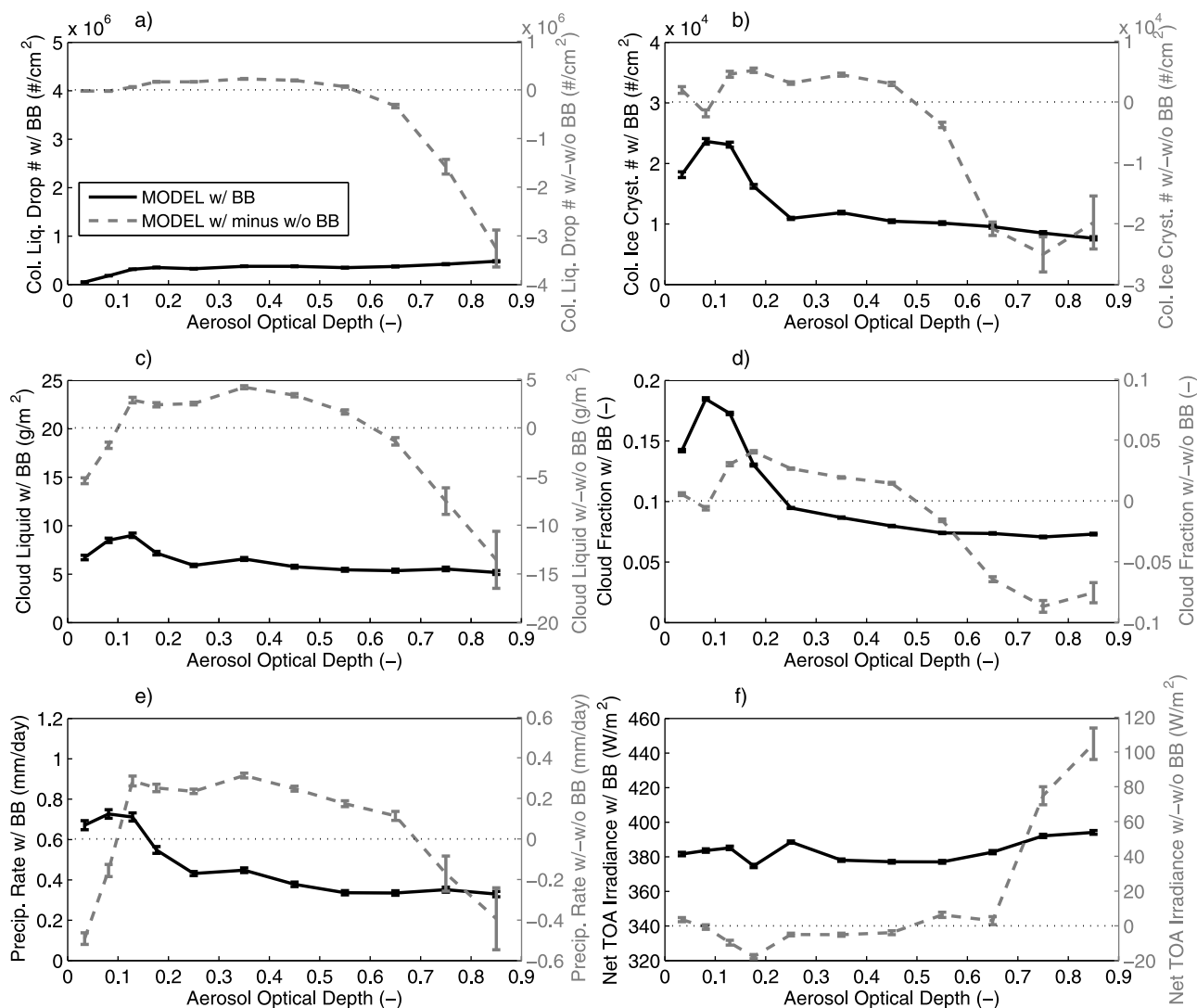


Figure 7. Model (a) column cloud liquid drop number, (b) column cloud ice crystal number, (c) column cloud liquid water, (d) cloud fraction, (e) precipitation rate, and (f) net TOA downward solar+IR irradiance binned by model AOD at $0.55 \mu\text{m}$ over all grid cells and daytime hours of the simulation in domain D4. Black lines represent the simulation w/ BB and gray lines represent the simulation w/ BB minus the simulation w/o BB. Error bars are calculated similarly to Figure 6. The scale interval is similar between the left and right y axes for comparison purposes.

observational studies [Jiang *et al.*, 2008; Koren *et al.*, 2004], but disagrees with others depending on the year analyzed [Lin *et al.*, 2006; Yu *et al.*, 2007].

[38] Grey lines representing the differenced w/ BB and w/o BB simulations in Figure 7 provide the causal effect of the BB aerosols. In Figure 7a, radiative effects at AODs above ~ 0.6 in the simulation w/ BB reduce the number of column cloud liquid drops in the simulation w/ BB relative to the simulation w/o BB, even though the number of available CCN is higher. This negative change in cloud liquid drop number with increasing AOD is consistent with the strong radiative effect on COD shown in Figure 6b – the lower relative humidity and reduced surface fluxes in the simulation w/ BB relative to the simulation w/o BB result in a reduction in the number of cloud liquid drops and COD. Figure 7b shows a similar behavior for column cloud ice

crystal number, with a positive change at low AODs due to the greater number of available IDN in the simulation w/ BB, followed by a negative change at higher AODs. In Figures 7b–7e, cloud and precipitation variables are higher in the simulation w/ BB compared to the simulation w/o BB for AODs between ~ 0.1 and ~ 0.5 – 0.7 , and are lower for AODs above ~ 0.5 – 0.7 . Similar to Figure 6b, radiative effects may begin to dominate in the simulation w/ BB at a lower AOD than ~ 0.5 – 0.7 for variables in Figures 7b–7e, as shown by the changing slope of the curves at an AOD of ~ 0.1 in the simulation w/ BB. At an AOD of ~ 0.5 – 0.7 , radiative effects offset the stronger microphysical effect in the simulation w/ BB, changing the values of the w/ BB minus w/o BB curves from positive to negative. In Figures 7c and 7e, these w/ BB minus w/o BB curves are negative at very low AODs ($< \sim 0.1$) possibly due to the larger fraction of small aerosol

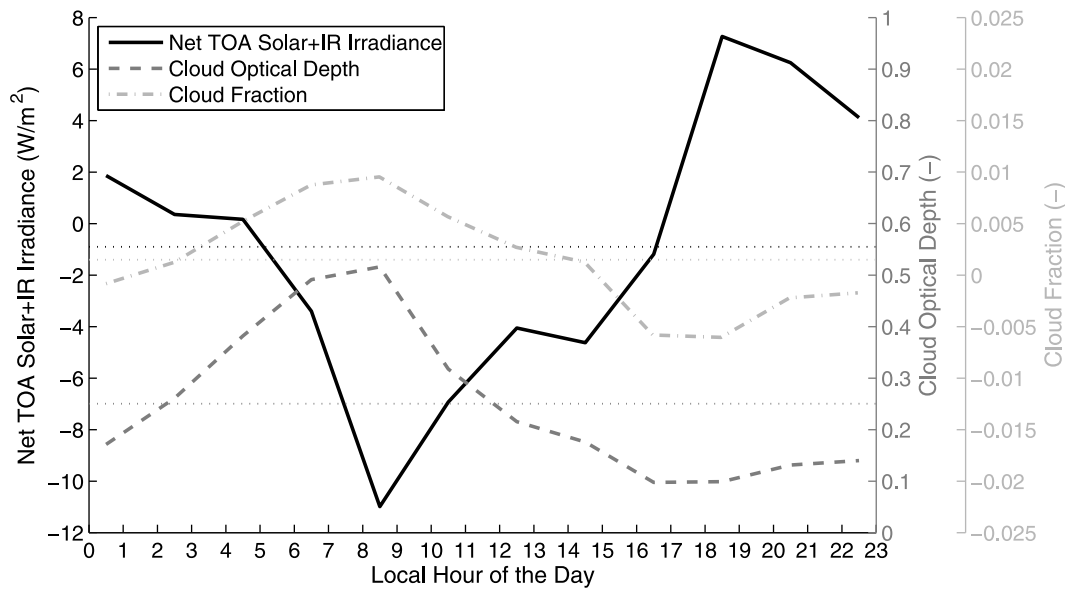


Figure 8. Diurnal time series of the area-weighted domain-averaged difference in net TOA downward irradiance, domain-averaged COD (including clear sky regions), and cloud fraction between simulations w/ BB and w/o BB in domain D4. For each hour, results from all grid cells and all days of the simulation during that hour are averaged. The lower dotted line represents the mean COD difference over all hours (+0.25), the middle dotted line represents the mean cloud fraction difference (+0.0015), and the upper dotted line represents the mean net TOA irradiance difference (-0.90 W/m^2) over the simulation and domain.

particles that do not activate as readily in the simulation w/ BB compared to the simulation w/o BB, similar to Figure 6b.

[39] Can aerosol washout/rainout play a role in these aerosol-cloud relationships? Thicker clouds may result in more precipitation and higher aerosol washout/rainout rates, resulting in a negative relationship between aerosols and clouds, yet we find that when the effect of washout/rainout is removed in the model, similar increasing followed by decreasing relationships between cloud variables and aerosol loading are still present, suggesting that washout/rainout has a minimal effect (see auxiliary material Figures S3 and S4). This two regime relationship shown in Figures 6 and 7 also agrees with a cloud-resolving large eddy simulation of warm clouds over the Amazon [Jiang and Feingold, 2006]. In the study, COD was shown to initially increase with increasing aerosol number concentration, and then decrease with increasing aerosol number concentration at higher aerosol concentrations due to radiative feedbacks of aerosols that stabilize the sub-cloud layer and reduce surface fluxes at high aerosol loadings, similar to results found here. Furthermore, surface temperature, the number of liquid cloud drops, cloud fraction, and cloud liquid water all become increasingly more negative with increasing aerosol number concentration for simulations w/ minus w/o radiative effects, again similar to results shown here [Jiang and Feingold, 2006]. The Jiang and Feingold [2006] study only modeled warm clouds, but our mixed-phase simulations show similar results since (1) many of the clouds in our simulation are warm clouds (auxiliary material Figure S1) and (2) a similar two regime behavior appears to exist for ice clouds as well (Figure 7b). Strong similarities between modeling results in

this study and the cloud-resolving study of Jiang and Feingold [2006], along with similarities to remote sensing observations, suggest that the aerosol-cloud relationships presented in this study are physically based and that the critical microphysical, radiative, and dynamical processes that determine the effects of aerosols on clouds in this region and season are adequately simulated by the model.

[40] Figure 7f shows the impact of competing aerosol effects on the radiative balance of the atmosphere. In the differenced w/ BB minus w/o BB simulation, we find a largely negative change (up to -18 W/m^2) in the net TOA downward solar+IR irradiance for AODs below ~ 0.5 . This corresponds to an earth-atmosphere cooling in the simulation w/ BB compared to the simulation w/o BB as a negative irradiance change represents net energy removed from the earth-atmosphere system. However, at AODs higher than ~ 0.5 , the reduction in COD and cloud fraction shown in Figure 6b and Figure 7d, respectively, results in a positive change in the TOA irradiance up to 100 W/m^2 . The radiative effect of aerosols produces a greater relative warming at high AODs compared to the cooling produced at lower AODs; however, these high AOD scenarios occur less frequently than lower AOD scenarios. In Figure 7f, 69% of the total COD-AOD pairs in the simulation w/ BB and 95% of the pairs in the simulation w/o BB produce a negative TOA irradiance change ($< \sim 0.5$ AOD) whereas the remaining fewer pairs produce a positive TOA irradiance change ($> \sim 0.5$ AOD) (auxiliary material Table S3).

[41] Figure 8 further probes the competition between aerosol microphysical and radiative effects and their net impact on the regional radiative balance by analyzing the

domain-averaged diurnal variation of the differences in COD, cloud fraction, and net TOA solar+IR irradiance between simulations w/ BB and w/o BB. From 0:00 LT until sunrise, aerosol microphysical effects in the absence of sunlight increase COD and cloud fraction in the simulation w/ BB relative to the simulation w/o BB. A corresponding positive change in the net TOA solar+IR irradiance is detected as aerosols, gases, and clouds absorb and scatter IR. After sunrise, the net TOA irradiance difference changes from positive to negative as cloud fields that are brighter and cover a larger fraction of the sky reflect more solar radiation in the simulation w/ BB relative to the simulation w/o BB. This irradiance change is most negative (-11 W/m^2) when the COD and cloud fraction difference is greatest at 8:00–9:00 LT. After this time, radiative effects begin to play a larger role as the incoming solar flux increases, and the positive COD/cloud fraction change begins to diminish. The net TOA irradiance difference changes from negative to positive at 16:00–17:00 LT as radiative effects increase in magnitude relative to microphysical effects. This positive irradiance change is maximized ($+7.3 \text{ W/m}^2$) when the difference in COD/cloud fraction is minimized at 18:00–19:00 LT during early evening. The COD begins to increase again after sunset and the net TOA irradiance remains above zero throughout the night. Over the averaged simulated day, a radiative flux change of -0.90 W/m^2 is found, implying an overall net cooling due to BB.

[42] These results are consistent with a modeling study over the Amazon using WRF-Chem [Wu *et al.*, 2011], which shows a similar BB-induced diurnal cycle in clouds attributed to competing microphysical and radiative effects of aerosols. Yet, it should be stated that these irradiance changes are somewhat uncertain since the model simulates cloud ensembles rather than individual clouds. For instance, squall lines resulting from the dynamical-microphysical feedback of aerosols to convective outflows and new convective initiation will not be adequately resolved in these simulations [Khain *et al.*, 2005]. It has been shown that the effect of aerosols on convective systems may be different than the effect on isolated deep convection [Khain, 2009]. Furthermore, convective anvils, which may have a large impact on the radiative balance, are not resolved in this study. Cloud invigoration over the Atlantic and Pacific Oceans has been observed to result in an increase in the total and anvil cloud fraction, a decrease in the tower size to anvil size ratio, and consequently an increase in the TOA downward irradiance [Koren *et al.*, 2010b]. However, the majority of clouds that form in this region and season are shallow cumuli that do not contain anvils. Nevertheless, cloud-resolving simulations are needed to accurately model cloud-scale effects, making the results presented here somewhat uncertain. The simulation-averaged radiative flux change found here is similar to the value of -0.84 W/m^2 found due to BB aerosol effects in a previous study using GATOR-GCMOM [Jacobson, 2004], and is consistent with regional values of the total aerosol effect over South America from other global modeling experiments [Bauer *et al.*, 2010; Koch *et al.*, 2011].

[43] These findings suggest that the time of the day may have a substantial impact on the radiative forcing of BB emissions. This analysis assumes a constant rate of BB emissions throughout the day. Additional studies are

required to assess the impact of a more realistic diurnally varying BB emission rate on these opposing microphysical and radiative aerosol effects [Giglio, 2007]; however, this impact is assumed to be small since the average lifetime of aerosol emissions in the atmosphere is significantly longer than one day.

4. Conclusions

[44] This study analyzes the influence of biomass burning (BB) aerosols on mixed-phase clouds, precipitation, and the regional radiative balance through simulations that included and excluded BB during the peak of the 2006 Amazon fire season. The climate-air pollution-weather forecast model, GATOR-GCMOM, which contains physical treatment of aerosol-cloud microphysical and radiative (semi-direct and cloud absorption) effects, was used. A global domain at $4.0^\circ \text{ NS} \times 5.0^\circ \text{ WE}$ resolution and three nested domains ranging between resolutions of $1.0^\circ \text{ NS} \times 1.0^\circ \text{ WE}$ and $0.2^\circ \text{ NS} \times 0.2^\circ \text{ WE}$ were employed over the heaviest BB region in the arc of deforestation. Comparisons with MODIS Aqua and TRMM observations show that the model predicts AOD, COD, column water vapor, cloud top pressure, and precipitation rate rather well over the simulation domain and period. We also find that the model accurately predicts upper-air and surface meteorological variables paired in time and space. Finally, comparisons between AERONET and model AOD and SSA for several stations in the domain are also shown to be consistent.

[45] Previous observational, theoretical, and cloud-resolving modeling studies have suggested there may be a smooth transition between aerosol microphysical and radiative effects. We compare correlations between cloud-averaged COD and AOD developed using a physical GCM with remotely sensed MODIS correlations between COD and AOD over the Amazon Basin. We find that in agreement with earlier studies both observations and model results suggest an increase in COD with increasing AOD for AODs below ~ 0.3 due to a combination of aerosol microphysical effects and destabilization of the atmosphere above the aerosol layer from aerosol heating, whereas COD decreases with increasing AOD for AODs between ~ 0.3 and 0.9 due to radiative effects which evaporate clouds and stabilize the lower boundary layer, reducing surface sensible and latent heat fluxes. The similarity between MODIS observations and model results suggest that these correlations are physically based, and are not dominated by satellite retrieval artifacts such as the brightening of aerosols near clouds, cloud contamination of aerosol, or artificial darkening of clouds below an absorbing aerosol layer. A similar increasing followed by decreasing relationship was found between cloud-averaged COD and dry aerosol mass in the model, suggesting that aerosol humidification is also not dominant in this AOD range. Furthermore, the agreement of this result with other observational and cloud-resolving modeling studies conducted at different resolutions with varying levels of detail points to the robustness of this two regime relationship and suggests that the critical microphysical, radiative, and dynamical processes that determine the effect of aerosols on clouds in this region and season are simulated acceptably well at the scales employed in our model experiments.

[46] Correlations, however, can be affected by changes to the background meteorology over the simulation period and domain and thus do not represent the isolated effect of the BB. To study the causal effect of BB, differences between simulations w/ BB and w/o BB were analyzed. Increases in simulation- and domain-averaged column ice crystal number, column cloud ice, and lightning flashes in the simulation w/ BB compared to the simulation w/o BB suggest an overall invigoration of cold cloud processes. We also find that COD, column cloud liquid drop number, column cloud ice crystal number, column cloud liquid water, cloud fraction, and precipitation are generally higher in the simulation w/ BB than in the simulation w/o BB for AODs below ~ 0.5 – 0.7 . At AODs between ~ 0.5 – 0.7 and 0.9 , we find these variables are lower for the simulation w/ BB compared to the simulation w/o BB. The AOD threshold at which the simulation w/ BB minus w/o BB changes from positive to negative (~ 0.5 – 0.7) is higher than the AOD threshold at which radiative effects begin to dominate microphysical effects in the simulation w/ BB (~ 0.1 – 0.3). This is because the simulation w/ BB exhibits an enhanced microphysical and radiative effect compared to the simulation w/o BB. For the radiative effect to offset the stronger microphysical effect in the simulation w/ BB, the AOD threshold at which the simulation w/ BB minus w/o BB changes from positive to negative must be higher than the AOD threshold at which radiative effects begin to dominate microphysical effects in the simulation w/ BB. Altogether, we find that the total aerosol effect is a sum of both microphysical and radiative effects that vary in magnitude for different degrees of aerosol loading.

[47] The impact of competing aerosol microphysical and radiative effects on the regional radiative balance is also studied. Correlations between the net TOA downward solar+IR irradiance and AOD differenced between the simulations w/ BB and w/o BB show that microphysical effects decrease the radiative flux into the earth-atmosphere system at AODs below ~ 0.5 (earth-atmosphere cooling), whereas radiative effects dramatically increase the radiative flux into the earth-atmosphere system at higher AODs (earth-atmosphere warming), yet these high AOD conditions occur less frequently. We also find that microphysical effects dominate in the early morning, decreasing the net TOA solar+IR irradiance relative to the simulation w/o BB. Radiative effects are found to grow in strength throughout the day until they dominate microphysical effects by late afternoon, switching the net effect of BB aerosols from cooling to warming relative to the simulation w/o BB. Averaged over all hours of the simulation, we find that BB results in a net TOA solar+IR radiative flux change of -0.90 W/m^2 , with an average peak cooling of -11 W/m^2 in the morning and an average peak warming of $+7.3 \text{ W/m}^2$ in the early evening. Thus, the time of day is found to have a large impact on the radiative forcing of BB emissions. It should be stated, however, that the magnitudes of these radiative flux changes are somewhat uncertain due to uncertainties in the parameterization of convection in the model.

[48] **Acknowledgments.** We thank Brent Holben and Paulo Artaxo for establishing and maintaining the eight AERONET sites used in this investigation. We also thank James T. Randerson for providing access to the GFEDv2 database. This work was sponsored by the Stanford University Graduate Fellowship, the NASA Earth System Science Fellowship, the

NASA High-End Computing Center, NASA grant NN07AN25G, and U.S. EPA grant RD-83337101-O.

References

- Ackerman, A. S., O. B. Toon, D. E. Stevens, A. J. Heymsfield, V. Ramanathan, and E. J. Welton (2000), Reduction of tropical cloudiness by soot, *Science*, 288(5468), 1042–1047, doi:10.1126/science.288.5468.1042.
- Albrecht, B. A. (1989), Aerosols, cloud microphysics, and fractional cloudiness, *Science*, 245(4923), 1227–1230, doi:10.1126/science.245.4923.1227.
- Andreae, M. O. (2009), Correlation between cloud condensation nuclei concentration and aerosol optical thickness in remote and polluted regions, *Atmos. Chem. Phys.*, 9(2), 543–556, doi:10.5194/acp-9-543-2009.
- Andreae, M. O., and P. Merlet (2001), Emission of trace gases and aerosols from biomass burning, *Global Biogeochem. Cycles*, 15(4), 955–966, doi:10.1029/2000GB001382.
- Andreae, M. O., D. Rosenfeld, P. Artaxo, A. A. Costa, G. P. Frank, K. M. Longo, and M. A. F. Silva-Dias (2004), Smoking rain clouds over the Amazon, *Science*, 303(5662), 1337–1342, doi:10.1126/science.1092779.
- Arakawa, A., and V. R. Lamb (1981), A potential enstrophy and energy conserving scheme for the shallow-water equations, *Mon. Weather Rev.*, 109(1), 18–36, doi:10.1175/1520-0493(1981)109<0018:APEAEC>2.0.CO;2.
- Bauer, S. E., S. Menon, D. Koch, T. C. Bond, and K. Tsigaridis (2010), A global modeling study on carbonaceous aerosol microphysical characteristics and radiative effects, *Atmos. Chem. Phys.*, 10(15), 7439–7456, doi:10.5194/acp-10-7439-2010.
- Bergstrom, R. W., and R. Viskanta (1973), Modeling of the effects of gaseous and particulate pollutants in the urban atmosphere. Part I: Thermal structure, *J. Appl. Meteorol.*, 12(6), 901–912, doi:10.1175/1520-0450(1973)012<0901:MOTEOG>2.0.CO;2.
- Bond, T. C., G. Habib, and R. W. Bergstrom (2006), Limitations in the enhancement of visible light absorption due to mixing state, *J. Geophys. Res.*, 111, D20211, doi:10.1029/2006JD007315.
- Brennan, J. I., Y. J. Kaufman, I. Koren, and R. R. Li (2005), Aerosol-cloud interaction-misclassification of MODIS clouds in heavy aerosol, *IEEE Trans. Geosci. Remote Sens.*, 43(4), 911–915, doi:10.1109/TGRS.2005.844662.
- Chýlek, P., G. B. Lesins, G. Videen, J. G. D. Wong, R. G. Pinnick, D. Ngo, and J. D. Klett (1996), Black carbon and absorption of solar radiation by clouds, *J. Geophys. Res.*, 101(D18), 23,365–23,371, doi:10.1029/96JD01901.
- Coakley, J. A., R. D. Cess, and F. B. Yurevich (1983), The effect of tropospheric aerosols on the Earth's radiation budget—A parameterization for climate models, *J. Atmos. Sci.*, 40(1), 116–138, doi:10.1175/1520-0469(1983)040<0116:TEOTAO>2.0.CO;2.
- Conant, W. C., A. Nenes, and J. H. Seinfeld (2002), Black carbon radiative heating effects on cloud microphysics and implications for the aerosol indirect effect: 1. Extended Kohler theory, *J. Geophys. Res.*, 107(D21), 4604, doi:10.1029/2002JD002094.
- Danielson, R. E., D. R. Moore, and H. C. van de Hulst (1969), The transfer of visible radiation through clouds, *J. Atmos. Sci.*, 26(5), 1078–1087, doi:10.1175/1520-0469(1969)026<1078:TTOVRT>2.0.CO;2.
- Davidi, A., I. Koren, and L. Remer (2009), Direct measurements of the effect of biomass burning over the Amazon on the atmospheric temperature profile, *Atmos. Chem. Phys.*, 9(21), 8211–8221, doi:10.5194/acp-9-8211-2009.
- Defries, R. S., and J. R. G. Townshend (1994), NDVI-derived land cover classifications at a global scale, *Int. J. Remote Sens.*, 15(17), 3567–3586, doi:10.1080/01431169408954345.
- Dey, S., L. Di Girolamo, G. Zhao, A. L. Jones, and G. M. McFarquhar (2011), Satellite-observed relationships between aerosol and trade-wind cumulus cloud properties over the Indian Ocean, *Geophys. Res. Lett.*, 38, L01804, doi:10.1029/2010GL045588.
- Ding, P., and D. A. Randall (1998), A cumulus parameterization with multiple cloud base levels, *J. Geophys. Res.*, 103(D10), 11,341–11,353, doi:10.1029/98JD00346.
- Dubovik, O., and M. D. King (2000), A flexible inversion algorithm for retrieval of aerosol optical properties from Sun and sky radiance measurements, *J. Geophys. Res.*, 105(D16), 20,673–20,696, doi:10.1029/2000JD900282.
- Dubovik, O., B. Holben, T. F. Eck, A. Smirnov, Y. J. Kaufman, M. D. King, D. Tanre, and I. Slutsker (2002), Variability of absorption and optical properties of key aerosol types observed in worldwide locations, *J. Atmos. Sci.*, 59(3), 590–608, doi:10.1175/1520-0469(2002)059<0590:VOAOP>2.0.CO;2.

- Durre, I., R. S. Vose, and D. B. Wuertz (2006), Overview of the Integrated Global Radiosonde Archive, *J. Clim.*, *19*(1), 53–68, doi:10.1175/JCLI3594.1.
- Eck, T. F., B. N. Holben, J. S. Reid, O. Dubovik, A. Smirnov, N. T. O'Neill, I. Slutsker, and S. Kinne (1999), Wavelength dependence of the optical depth of biomass burning, urban, and desert dust aerosols, *J. Geophys. Res.*, *104*(D24), 31,333–31,349, doi:10.1029/1999JD900923.
- Eck, T. F., B. N. Holben, J. S. Reid, N. T. O'Neill, J. S. Schafer, O. Dubovik, A. Smirnov, M. A. Yamasoe, and P. Artaxo (2003), High aerosol optical depth biomass burning events: A comparison of optical properties for different source regions, *Geophys. Res. Lett.*, *30*(20), 2035, doi:10.1029/2003GL017861.
- Fan, Y., and H. van den Dool (2004), Climate Prediction Center global monthly soil moisture data set at 0.5° resolution for 1948 to present, *J. Geophys. Res.*, *109*, D10102, doi:10.1029/2003JD004345.
- Feingold, G., L. A. Remer, J. Ramaprasad, and Y. J. Kaufman (2001), Analysis of smoke impact on clouds in Brazilian biomass burning regions: An extension of Twomey's approach, *J. Geophys. Res.*, *106*(D19), 22,907–22,922, doi:10.1029/2001JD000732.
- Feingold, G., H. Jiang, and J. Y. Harrington (2005), On smoke suppression of clouds in Amazonia, *Geophys. Res. Lett.*, *32*, L02804, doi:10.1029/2004GL021369.
- Ferek, R. J., J. S. Reid, P. V. Hobbs, D. R. Blake, and C. Liousse (1998), Emission factors of hydrocarbons, halocarbons, trace gases and particles from biomass burning in Brazil, *J. Geophys. Res.*, *103*(D24), 32,107–32,118, doi:10.1029/98JD00692.
- Food and Agriculture Organization (1996), *Soil Map of the World [CD-ROM]*, Land and Water Dev. Div., Rome, Italy.
- Forster, P., et al. (2007), Radiative forcing of climate change, in *Climate Change 2007: The Physical Science Basis. Contribution of Working Group I to the Fourth Assessment Report of the Intergovernmental Panel on Climate Change*, edited by S. Solomon et al., pp. 351–416, Cambridge Univ. Press, Cambridge, U. K.
- Friedl, M. A., D. Sulla-Menashe, B. Tan, A. Schneider, N. Ramankutty, A. Sibley, and X. M. Huang (2010), MODIS Collection 5 global land cover: Algorithm refinements and characterization of new datasets, *Remote Sens. Environ.*, *114*(1), 168–182, doi:10.1016/j.rse.2009.08.016.
- Giglio, L. (2007), Characterization of the tropical diurnal fire cycle using VIRS and MODIS observations, *Remote Sens. Environ.*, *108*(4), 407–421, doi:10.1016/j.rse.2006.11.018.
- Giglio, L., J. Descloitres, C. O. Justice, and Y. J. Kaufman (2003), An enhanced contextual fire detection algorithm for MODIS, *Remote Sens. Environ.*, *87*(2–3), 273–282, doi:10.1016/S0034-4257(03)00184-6.
- Giglio, L., G. R. van der Werf, J. T. Randerson, G. J. Collatz, and P. Kasibhatla (2006), Global estimation of burned area using MODIS active fire observations, *Atmos. Chem. Phys.*, *6*, 957–974, doi:10.5194/acp-6-957-2006.
- Grassl, H. (1975), Albedo reduction and radiative heating of clouds by absorbing aerosol particles, *Contrib. Atmos. Phys.*, *48*, 199–210.
- Gunn, R., and B. B. Phillips (1957), An experimental investigation of the effect of air pollution on the initiation of rain, *J. Atmos. Sci.*, *14*, 272–280.
- Hansen, J., M. Sato, and R. Ruedy (1997), Radiative forcing and climate response, *J. Geophys. Res.*, *102*(D6), 6831–6864, doi:10.1029/96JD03436.
- Holben, B. N., et al. (1998), AERONET—A federated instrument network and data archive for aerosol characterization, *Remote Sens. Environ.*, *66*(1), 1–16, doi:10.1016/S0034-4257(98)00031-5.
- Huete, A., K. Didan, T. Miura, E. P. Rodriguez, X. Gao, and L. G. Ferreira (2002), Overview of the radiometric and biophysical performance of the MODIS vegetation indices, *Remote Sens. Environ.*, *83*(1–2), 195–213, doi:10.1016/S0034-4257(02)00096-2.
- Huffman, G. J., R. F. Adler, D. T. Bolvin, G. J. Gu, E. J. Nelkin, K. P. Bowman, Y. Hong, E. F. Stocker, and D. B. Wolff (2007), The TRMM multisatellite precipitation analysis (TMPA): Quasi-global, multiyear, combined-sensor precipitation estimates at fine scales, *J. Hydrometeorol.*, *8*(1), 38–55, doi:10.1175/JHM560.1.
- Jacobson, M. Z. (1997), Development and application of a new air pollution modeling system. Part III. Aerosol-phase simulations, *Atmos. Environ.*, *31*(7), 587–608, doi:10.1016/S1352-2310(97)80972-7.
- Jacobson, M. Z. (1998), Studying the effects of aerosols on vertical photolysis rate coefficient and temperature profiles over an urban airshed, *J. Geophys. Res.*, *103*(D9), 10,593–10,604, doi:10.1029/98JD00287.
- Jacobson, M. Z. (1999), Isolating nitrated and aromatic aerosols and nitrated aromatic gases as sources of ultraviolet light absorption, *J. Geophys. Res.*, *104*(D3), 3527–3542, doi:10.1029/1998JD100054.
- Jacobson, M. Z. (2001a), GATOR-GCMM: A global- through urban-scale air pollution and weather forecast model: 1. Model design and treatment of subgrid soil, vegetation, roads, rooftops, water, sea ice, and snow, *J. Geophys. Res.*, *106*(D6), 5385–5401, doi:10.1029/2000JD900560.
- Jacobson, M. Z. (2001b), Global direct radiative forcing due to multicomponent anthropogenic and natural aerosols, *J. Geophys. Res.*, *106*(D2), 1551–1568, doi:10.1029/2000JD900514.
- Jacobson, M. Z. (2001c), Strong radiative heating due to the mixing state of black carbon in atmospheric aerosols, *Nature*, *409*(6821), 695–697, doi:10.1038/35055518.
- Jacobson, M. Z. (2002a), Control of fossil-fuel particulate black carbon and organic matter, possibly the most effective method of slowing global warming, *J. Geophys. Res.*, *107*(D19), 4410, doi:10.1029/2001JD001376.
- Jacobson, M. Z. (2002b), Analysis of aerosol interactions with numerical techniques for solving coagulation, nucleation, condensation, dissolution, and reversible chemistry among multiple size distributions, *J. Geophys. Res.*, *107*(D19), 4366, doi:10.1029/2001JD002044.
- Jacobson, M. Z. (2003), Development of mixed-phase clouds from multiple aerosol size distributions and the effect of the clouds on aerosol removal, *J. Geophys. Res.*, *108*(D8), 4245, doi:10.1029/2002JD002691.
- Jacobson, M. Z. (2004), The short-term cooling but long-term global warming due to biomass burning, *J. Clim.*, *17*(15), 2909–2926, doi:10.1175/1520-0442(2004)017<2909:TSCBLG>2.0.CO;2.
- Jacobson, M. Z. (2005), A refined method of parameterizing absorption coefficients among multiple gases simultaneously from line-by-line data, *J. Atmos. Sci.*, *62*(2), 506–517, doi:10.1175/JAS-3372.1.
- Jacobson, M. Z. (2006), Effects of externally through-internally mixed soot inclusions within clouds and precipitation on global climate, *J. Phys. Chem. A*, *110*(21), 6860–6873, doi:10.1021/jp056391r.
- Jacobson, M. Z. (2010), Short-term effects of controlling fossil-fuel soot, biofuel soot and gases, and methane on climate, Arctic ice, and air pollution health, *J. Geophys. Res.*, *115*, D14209, doi:10.1029/2009JD013795.
- Jacobson, M. Z., Y. J. Kaufman, and Y. Rudich (2007), Examining feedbacks of aerosols to urban climate with a model that treats 3-D clouds with aerosol inclusions, *J. Geophys. Res.*, *112*, D24205, doi:10.1029/2007JD008922.
- Janhäll, S., M. O. Andreae, and U. Poschl (2010), Biomass burning aerosol emissions from vegetation fires: Particle number and mass emission factors and size distributions, *Atmos. Chem. Phys.*, *10*(3), 1427–1439, doi:10.5194/acp-10-1427-2010.
- Jiang, H. L., and G. Feingold (2006), Effect of aerosol on warm convective clouds: Aerosol-cloud-surface flux feedbacks in a new coupled large eddy model, *J. Geophys. Res.*, *111*, D01202, doi:10.1029/2005JD006138.
- Jiang, J. H., H. Su, M. R. Schoeberl, S. T. Massie, P. Colarco, S. Platnick, and N. J. Livesey (2008), Clean and polluted clouds: Relationships among pollution, ice clouds, and precipitation in South America, *Geophys. Res. Lett.*, *35*, L14804, doi:10.1029/2008GL034631.
- Jones, T. A., S. A. Christopher, and J. Quaas (2009), A six year satellite-based assessment of the regional variations in aerosol indirect effects, *Atmos. Chem. Phys.*, *9*(12), 4091–4114, doi:10.5194/acp-9-4091-2009.
- Kalnay, E., et al. (1996), The NCEP/NCAR 40-Year Reanalysis Project, *Bull. Am. Meteorol. Soc.*, *77*(3), 437–471, doi:10.1175/1520-0477(1996)077<0437:TNYRP>2.0.CO;2.
- Kaufman, Y. J., and R. S. Fraser (1997), The effect of smoke particles on clouds and climate forcing, *Science*, *277*(5332), 1636–1639, doi:10.1126/science.277.5332.1636.
- Kaufman, Y. J., and I. Koren (2006), Smoke and pollution aerosol effect on cloud cover, *Science*, *313*(5787), 655–658, doi:10.1126/science.1126232.
- Kaufman, Y. J., I. Koren, L. A. Remer, D. Rosenfeld, and Y. Rudich (2005a), The effect of smoke, dust, and pollution aerosol on shallow cloud development over the Atlantic Ocean, *Proc. Natl. Acad. Sci. U. S. A.*, *102*(32), 11,207–11,212, doi:10.1073/pnas.0505191102.
- Kaufman, Y. J., et al. (2005b), A critical examination of the residual cloud contamination and diurnal sampling effects on MODIS estimates of aerosol over ocean, *IEEE Trans. Geosci. Remote Sens.*, *43*(12), 2886–2897, doi:10.1109/TGRS.2005.858430.
- Keyser, D., and R. A. Anthes (1977), Applicability of a mixed-layer model of planetary boundary-layer to real-data forecasting, *Mon. Weather Rev.*, *105*(11), 1351–1371, doi:10.1175/1520-0493(1977)105<1351:TAOAMM>2.0.CO;2.
- Khain, A. P. (2009), Notes on state-of-the-art investigations of aerosol effects on precipitation: A critical review, *Environ. Res. Lett.*, *4*(1), 015004, doi:10.1088/1748-9326/4/1/015004.
- Khain, A., D. Rosenfeld, and A. Pokrovsky (2005), Aerosol impact on the dynamics and microphysics of deep convective clouds, *Q. J. R. Meteorol. Soc.*, *131*(611), 2639–2663, doi:10.1256/qj.04.62.
- Koch, D., and A. D. Del Genio (2010), Black carbon semi-direct effects on cloud cover: Review and synthesis, *Atmos. Chem. Phys.*, *10*(16), 7685–7696, doi:10.5194/acp-10-7685-2010.
- Koch, D., et al. (2011), Soot microphysical effects on liquid clouds, a multi-model investigation, *Atmos. Chem. Phys.*, *11*(3), 1051–1064, doi:10.5194/acp-11-1051-2011.

- Koren, I., Y. J. Kaufman, L. A. Remer, and J. V. Martins (2004), Measurement of the effect of Amazon smoke on inhibition of cloud formation, *Science*, 303(5662), 1342–1345, doi:10.1126/science.1089424.
- Koren, I., Y. J. Kaufman, D. Rosenfeld, L. A. Remer, and Y. Rudich (2005), Aerosol invigoration and restructuring of Atlantic convective clouds, *Geophys. Res. Lett.*, 32, L14828, doi:10.1029/2005GL023187.
- Koren, I., J. V. Martins, L. A. Remer, and H. Afargan (2008), Smoke invigoration versus inhibition of clouds over the Amazon, *Science*, 321(5891), 946–949, doi:10.1126/science.1159185.
- Koren, I., G. Feingold, and L. A. Remer (2010a), The invigoration of deep convective clouds over the Atlantic: Aerosol effect, meteorology or retrieval artifact?, *Atmos. Chem. Phys.*, 10(18), 8855–8872, doi:10.5194/acp-10-8855-2010.
- Koren, I., L. A. Remer, O. Altaratz, J. V. Martins, and A. Davidi (2010b), Aerosol-induced changes of convective cloud anvils produce strong climate warming, *Atmos. Chem. Phys.*, 10(10), 5001–5010, doi:10.5194/acp-10-5001-2010.
- Kummerow, C., W. Barnes, T. Kozu, J. Shiue, and J. Simpson (1998), The Tropical Rainfall Measuring Mission (TRMM) sensor package, *J. Atmos. Oceanic Technol.*, 15(3), 809–817, doi:10.1175/1520-0426(1998)015<0809:TTRMMT>2.0.CO;2.
- Levy, R. C., L. A. Remer, R. G. Kleidman, S. Mattoo, C. Ichoku, R. Kahn, and T. F. Eck (2010), Global evaluation of the Collection 5 MODIS dark-target aerosol products over land, *Atmos. Chem. Phys.*, 10(21), 10399–10420, doi:10.5194/acp-10-10399-2010.
- Lin, J. C., T. Matsui, R. A. Pielke, and C. Kummerow (2006), Effects of biomass-burning-derived aerosols on precipitation and clouds in the Amazon Basin: A satellite-based empirical study, *J. Geophys. Res.*, 111, D19204, doi:10.1029/2005JD006884.
- Lindsey, D. T., and M. Fromm (2008), Evidence of the cloud lifetime effect from wildfire-induced thunderstorms, *Geophys. Res. Lett.*, 35, L22809, doi:10.1029/2008GL035680.
- Loeb, N. G., and G. L. Schuster (2008), An observational study of the relationship between cloud, aerosol and meteorology in broken low-level cloud conditions, *J. Geophys. Res.*, 113, D14214, doi:10.1029/2007JD009763.
- Lott, N., R. Baldwin, and P. Jones (2001), The FCC Integrated Surface Hourly Database—A new resource of global climate data, *Tech. Rep. 2001-01*, Natl. Clim. Data Cent., Asheville, N. C.
- Marshak, A., G. Wen, J. A. Coakley Jr., L. A. Remer, N. G. Loeb, and R. F. Cahalan (2008), A simple model for the cloud adjacency effect and the apparent bluing of aerosols near clouds, *J. Geophys. Res.*, 113, D14S17, doi:10.1029/2007JD009196.
- Martins, J. A., M. A. F. Silva Dias, and F. L. T. Gonçalves (2009), Impact of biomass burning aerosols on precipitation in the Amazon: A modeling case study, *J. Geophys. Res.*, 114, D02207, doi:10.1029/2007JD009587.
- Mauger, G. S., and J. R. Norris (2007), Meteorological bias in satellite estimates of aerosol-cloud relationships, *Geophys. Res. Lett.*, 34, L16824, doi:10.1029/2007GL029952.
- McFarquhar, G. M., and H. Wang (2006), Effects of aerosols on trade wind cumuli over the Indian Ocean: Model simulations, *Q. J. R. Meteorol. Soc.*, 132(616), 821–843, doi:10.1256/qj.04.179.
- Menon, S., J. Hansen, L. Nazarenko, and Y. F. Luo (2002), Climate effects of black carbon aerosols in China and India, *Science*, 297(5590), 2250–2253, doi:10.1126/science.1075159.
- Myhre, G., F. Stordal, M. Johnsrud, Y. J. Kaufman, D. Rosenfeld, T. Storelvmo, J. E. Kristjansson, T. K. Berntsen, A. Myhre, and I. S. A. Isaksen (2007), Aerosol-cloud interaction inferred from MODIS satellite data and global aerosol models, *Atmos. Chem. Phys.*, 7(12), 3081–3101, doi:10.5194/acp-7-3081-2007.
- Negri, A. J., R. F. Adler, L. M. Xu, and J. Surratt (2004), The impact of Amazonian deforestation on dry season rainfall, *J. Clim.*, 17(6), 1306–1319, doi:10.1175/1520-0442(2004)017<1306:TIOADO>2.0.CO;2.
- Nicholls, S. (1984), The dynamics of stratocumulus: Aircraft observations and comparisons with a mixed layer model, *Q. J. R. Meteorol. Soc.*, 110(466), 783–820, doi:10.1002/qj.49711046603.
- Nobre, C. A., L. F. Mattos, C. P. Derczynski, T. A. Tarasova, and I. V. Trosnikov (1998), Overview of atmospheric conditions during the Smoke, Clouds, and Radiation-Brazil (SCAR-B) field experiment, *J. Geophys. Res.*, 103(D24), 31,809–31,820, doi:10.1029/98JD00992.
- Pielke, R. A., Sr. (2002), *Mesoscale Meteorological Modeling*, Academic, San Diego, Calif.
- Platnick, S., M. D. King, S. A. Ackerman, W. P. Menzel, B. A. Baum, J. C. Riedi, and R. A. Frey (2003), The MODIS cloud products: Algorithms and examples from Terra, *IEEE Trans. Geosci. Remote Sens.*, 41(2), 459–473, doi:10.1109/TGRS.2002.808301.
- Quaas, J., O. Boucher, N. Bellouin, and S. Kinne (2008), Satellite-based estimate of the direct and indirect aerosol climate forcing, *J. Geophys. Res.*, 113, D05204, doi:10.1029/2007JD008962.
- Quaas, J., et al. (2009), Aerosol indirect effects—general circulation model intercomparison and evaluation with satellite data, *Atmos. Chem. Phys.*, 9(22), 8697–8717, doi:10.5194/acp-9-8697-2009.
- Quaas, J., B. Stevens, P. Stier, and U. Lohmann (2010), Interpreting the cloud cover–aerosol optical depth relationship found in satellite data using a general circulation model, *Atmos. Chem. Phys.*, 10(13), 6129–6135, doi:10.5194/acp-10-6129-2010.
- Ramanathan, V., C. Chung, D. Kim, T. Bettge, L. Buja, J. T. Kiehl, W. M. Washington, Q. Fu, D. R. Sikka, and M. Wild (2005), Atmospheric brown clouds: Impacts on South Asian climate and hydrological cycle, *Proc. Natl. Acad. Sci. U. S. A.*, 102(15), 5326–5333, doi:10.1073/pnas.0500656102.
- Randles, C. A., and V. Ramaswamy (2008), Absorbing aerosols over Asia: A Geophysical Fluid Dynamics Laboratory general circulation model sensitivity study of model response to aerosol optical depth and aerosol absorption, *J. Geophys. Res.*, 113, D21203, doi:10.1029/2008JD010140.
- Reid, J. S., and P. V. Hobbs (1998), Physical and optical properties of young smoke from individual biomass fires in Brazil, *J. Geophys. Res.*, 103(D24), 32,013–32,030, doi:10.1029/98JD00159.
- Remer, L. A., Y. J. Kaufman, B. N. Holben, A. M. Thompson, and D. McNamara (1998), Biomass burning aerosol size distribution and modeled optical properties, *J. Geophys. Res.*, 103(D24), 31,879–31,891, doi:10.1029/98JD00271.
- Remer, L. A., et al. (2005), The MODIS aerosol algorithm, products, and validation, *J. Atmos. Sci.*, 62(4), 947–973, doi:10.1175/JAS3385.1.
- Riggan, P. J., R. G. Tissell, R. N. Lockwood, J. A. Brass, J. A. R. Pereira, H. S. Miranda, A. C. Miranda, T. Campos, and R. Higgins (2004), Remote measurement of energy and carbon flux from wildfires in Brazil, *Ecol. Appl.*, 14(3), 855–872, doi:10.1890/02-5162.
- Rosenfeld, D., and W. L. Woodley (2000), Deep convective clouds with sustained supercooled liquid water down to -37.5°C , *Nature*, 405(6785), 440–442, doi:10.1038/35013030.
- Rosenfeld, D., U. Lohmann, G. B. Raga, C. D. O'Dowd, M. Kulmala, S. Fuzzi, A. Reissell, and M. O. Andreae (2008), Flood or drought: How do aerosols affect precipitation?, *Science*, 321(5894), 1309–1313, doi:10.1126/science.1160606.
- Seiler, W., and P. J. Crutzen (1980), Estimates of gross and net fluxes of carbon between the biosphere and the atmosphere from biomass burning, *Clim. Change*, 2(3), 207–247, doi:10.1007/BF00137988.
- Sekiguchi, M., T. Nakajima, K. Suzuki, K. Kawamoto, A. Higurashi, D. Rosenfeld, I. Sano, and S. Mukai (2003), A study of the direct and indirect effects of aerosols using global satellite data sets of aerosol and cloud parameters, *J. Geophys. Res.*, 108(D22), 4699, doi:10.1029/2002JD003359.
- Stevens, B., and G. Feingold (2009), Untangling aerosol effects on clouds and precipitation in a buffered system, *Nature*, 461(7264), 607–613, doi:10.1038/nature08281.
- Ten Hoeve, J. E., L. A. Remer, and M. Z. Jacobson (2011), Microphysical and radiative effects of aerosols on warm clouds during the Amazon biomass burning season as observed by MODIS: Impacts of water vapor and land cover, *Atmos. Chem. Phys.*, 11(7), 3021–3036, doi:10.5194/acp-11-3021-2011.
- Toon, O. B., C. P. McKay, T. P. Ackerman, and K. Santhanam (1989), Rapid calculation of radiative heating rates and photodissociation rates in inhomogeneous multiple-scattering atmospheres, *J. Geophys. Res.*, 94(D13), 16,287–16,301, doi:10.1029/JD094iD13p16287.
- Torres, O., Z. Chen, H. Jethva, C. Ahn, S. R. Freitas, and P. K. Bhartia (2010), OMI and MODIS observations of the anomalous 2008–2009 Southern Hemisphere biomass burning seasons, *Atmos. Chem. Phys.*, 10(8), 3505–3513, doi:10.5194/acp-10-3505-2010.
- Twohy, C. H., J. A. Coakley Jr., and W. R. Tahnk (2009), Effect of changes in relative humidity on aerosol scattering near clouds, *J. Geophys. Res.*, 114, D05205, doi:10.1029/2008JD010991.
- Twomey, S. (1977), Influence of pollution on shortwave albedo of clouds, *J. Atmos. Sci.*, 34(7), 1149–1152, doi:10.1175/1520-0469(1977)034<1149:TIOPOT>2.0.CO;2.
- Várnai, T., and A. Marshak (2009), MODIS observations of enhanced clear sky reflectance near clouds, *Geophys. Res. Lett.*, 36, L06807, doi:10.1029/2008GL037089.
- van der Werf, G. R., J. T. Randerson, L. Giglio, G. J. Collatz, P. S. Kasibhatla, and A. F. Arellano (2006), Interannual variability in global biomass burning emissions from 1997 to 2004, *Atmos. Chem. Phys.*, 6, 3423–3441, doi:10.5194/acp-6-3423-2006.
- van der Werf, G. R., J. T. Randerson, L. Giglio, G. J. Collatz, M. Mu, P. S. Kasibhatla, D. C. Morton, R. S. DeFries, Y. Jin, and T. T. van Leeuwen (2010), Global fire emissions and the contribution of deforestation, savanna, forest, agricultural, and peat fires (1997–2009), *Atmos. Chem. Phys.*, 10(23), 11,707–11,735, doi:10.5194/acp-10-11707-2010.

- Walcek, C. J. (2000), Minor flux adjustment near mixing ratio extremes for simplified yet highly accurate monotonic calculation of tracer advection, *J. Geophys. Res.*, *105*(D7), 9335–9348, doi:10.1029/1999JD901142.
- Ward, D. E., R. A. Susott, J. B. Kauffman, R. E. Babbitt, D. L. Cummings, B. Dias, B. N. Holben, Y. J. Kaufman, R. A. Rasmussen, and A. W. Setzer (1992), Smoke and fire characteristics for cerrado and deforestation burns in Brazil: Base-B Experiment, *J. Geophys. Res.*, *97*(D13), 14,601–14,619, doi:10.1029/92JD01218.
- Wen, G. Y., A. Marshak, and R. F. Cahalan (2006), Impact of 3-D clouds on clear-sky reflectance and aerosol retrieval in a biomass burning region of Brazil, *IEEE Geosci. Remote Sens.*, *3*(1), 169–172, doi:10.1109/LGRS.2005.861386.
- Wenze, Y., et al. (2006), MODIS leaf area index products: From validation to algorithm improvement, *IEEE Trans. Geosci. Remote Sens.*, *44*(7), 1885–1898, doi:10.1109/TGRS.2006.871215.
- Wilcox, E. M., Harshvardhan, and S. Platnick (2009), Estimate of the impact of absorbing aerosol over cloud on the MODIS retrievals of cloud optical thickness and effective radius using two independent retrievals of liquid water path, *J. Geophys. Res.*, *114*, D05210, doi:10.1029/2008JD010589.
- Williams, E., et al. (2002), Contrasting convective regimes over the Amazon: Implications for cloud electrification, *J. Geophys. Res.*, *107*(D20), 8082, doi:10.1029/2001JD000380.
- Wu, L., H. Su, and J. H. Jiang (2011), Regional simulations of deep convection and biomass burning over South America: 2. Biomass burning aerosol effects on clouds and precipitation, *J. Geophys. Res.*, *116*, D17209, doi:10.1029/2011JD016106.
- Yu, H., S. C. Liu, and R. E. Dickinson (2002), Radiative effects of aerosols on the evolution of the atmospheric boundary layer, *J. Geophys. Res.*, *107*(D12), 4142, doi:10.1029/2001JD000754.
- Yu, H., R. Fu, R. E. Dickinson, Y. Zhang, M. Chen, and H. Wang (2007), Interannual variability of smoke and warm cloud relationships in the Amazon as inferred from MODIS retrievals, *Remote Sens. Environ.*, *111*(4), 435–449, doi:10.1016/j.rse.2007.04.003.
- Yuan, T., Z. Li, R. Zhang, and J. Fan (2008), Increase of cloud droplet size with aerosol optical depth: An observation and modeling study, *J. Geophys. Res.*, *113*, D04201, doi:10.1029/2007JD008632.
- Zhang, Y., R. Fu, H. B. Yu, R. E. Dickinson, R. N. Juarez, M. Chin, and H. Wang (2008), A regional climate model study of how biomass burning aerosol impacts land-atmosphere interactions over the Amazon, *J. Geophys. Res.*, *113*, D14S15, doi:10.1029/2007JD009449.
- Zhang, Y., R. Fu, H. Yu, Y. Qian, R. Dickinson, M. A. F. Silva Dias, P. L. da Silva Dias, and K. Fernandes (2009), Impact of biomass burning aerosol on the monsoon circulation transition over Amazonia, *Geophys. Res. Lett.*, *36*, L10814, doi:10.1029/2009GL037180.

M. Z. Jacobson and J. E. Ten Hoeve, Department of Civil and Environmental Engineering, Stanford University, Stanford, CA 94305-4020, USA. (tenhoeve@stanford.edu)

L. A. Remer, Laboratory for Atmospheres, NASA Goddard Space Flight Center, Greenbelt, MD 20771, USA.